# Mechanical properties of quartz sand and gypsum powder (plaster) mixtures: implications for laboratory model analogues for the Earth's upper crust

**Sam Poppe**[1,2]*, Eoghan P. Holohan[3], Michael Rudolf[4], Matthias Rosenau[4], Olivier Galland[5], Audray Delcamp[1], Matthieu Kervyn[1]

1 Physical Geography, Department of Geography, Vrije Universiteit Brussel, Brussels, Belgium

2 now at Laboratoire G-Time, Department of Geoscience, the Environment and Society, Université Libre de Bruxelles, Brussels, Belgium

3 UCD School of Earth Sciences, University College of Dublin, Dublin 4, Ireland

4 Helmholtz Centre Potsdam - GFZ German Research Centre for Geosciences, Potsdam, Germany

5 Physics of Geological Processes, The Njord Center, University of Oslo, Oslo, Norway

***Corresponding author:** sam.poppe@ulb.be; sam35poppe@gmail.com

This manuscript has been submitted in TECTONOPHYSICS. Please note that the manuscript has not undergone peer-review yet and has yet to be formally accepted for publication. Subsequent versions of this manuscript may have slightly different content. If accepted, the final version of this manuscript will be available via the 'Peer-reviewed publication DOI' link on the right-hand side of this webpage. Please feel free to contact the authors, we welcome feedback.

**Title:**

# Mechanical properties of quartz sand and gypsum powder (plaster) mixtures: implications for laboratory model analogues for the Earth's upper crust

**Authors:**

**Sam Poppe**[1,2]*, Eoghan P. Holohan[3], Michael Rudolf[4], Matthias Rosenau[4], Olivier Galland[5], Audray Delcamp[1], Matthieu Kervyn[1]

1 Physical Geography, Department of Geography, Vrije Universiteit Brussel, Brussels, Belgium

2 now at Laboratoire G-Time, Department of Geoscience, the Environment and Society, Université Libre de Bruxelles, Brussels, Belgium

3 UCD School of Earth Sciences, University College of Dublin, Dublin 4, Ireland

4 Helmholtz Centre Potsdam - GFZ German Research Centre for Geosciences, Potsdam, Germany

5 Physics of Geological Processes, The Njord Center, University of Oslo, Oslo, Norway

***Corresponding author:** sam.poppe@ulb.be; sam35poppe@gmail.com

## Highlights

- Density, tensile strength, shear strength of sand-plaster mixtures quantified
- Cohesion and friction coefficients from Coulomb and Griffith failure criteria.
- Sensitivity to emplacement technique and ambient humidity.
- Brittle to ductile behaviour depending on plaster content and applied normal load.
- Tensile strength of sand-plaster mixtures as a scalable experimental parameter.

**Abstract**

Granular materials are a useful analogue for the Earth's crust in laboratory models of deformation. Constraining their mechanical properties is critical for such model's scaling and interpretation. Much information exists about monomineralic granular materials, such as quartz sand, but the mechanical characteristics of bimineralic mixtures, such as commonly-used quartz sand mixed with gypsum powder (i.e. plaster), are largely unconstrained. We used several mechanical tests (density, tensile, extension, shear) to constrain the failure envelope of various sand-plaster mixtures. We then fitted linear Coulomb and parabolic Griffith failure criteria to obtain cohesions and friction coefficients. Tests of the effects of emplacement technique, compaction and humidity demonstrated that the most reproducible rheology is given by oven-drying, pouring and mechanically compacting sand-plaster mixtures into their experimentation container. As plaster content increases, the tensile strength of dry sand-plaster mixtures increases from near zero (pure quartz sand) to 166±24 Pa (pure plaster). The cohesion increases from near zero to 250±21 Pa. The friction coefficient varies from 0.54±0.08 (sand) to 0.96±0.08 (20 weight% plaster). The mechanical behaviour of the resulting mixtures shifts at 20-35 weight% plaster from brittle Coulomb failure along a linear failure criterion, to more complex brittle-ductile Coulomb-Griffith failure along a non-linear failure criterion. With increasing plaster content, the brittle-ductile transition occurs at decreasing depth within a pile of sand-plaster mixture. We infer that the identified transitions in mechanical behaviour with increasing plaster content relate to (1) increasing porosities, (2) increasing grain size distributions, and (3) a decrease in sand-sand grain contacts and corresponding increase in gypsum-gypsum grain contacts. The presented characterisation enables a more quantitative scaling of the mechanical behaviour of sand-plaster mixtures, including of their tensile strength. Sand-plaster mixtures can thereby realistically simulate brittle-ductile properties of the Earth's crust in scaled laboratory models.

**Keywords:**

Laboratory modelling; Analogue materials; Quartz sand; Gypsum powder; Mechanical properties; Tensile strength; Shear strength; Cohesion; Friction coefficient

## 1. Introduction

The Earth's crust is a complex set of geological layers and structures, exhibiting a wide range of physical and mechanical properties. Properties such as rock density, porosity, tensile strength, shear strength, cohesion and internal friction control or relate to deformation of the crust during geological processes (Graveleau et al., 2012; Hubbert, 1951, e.g. 1937; Labuz et al., 2018). The mechanical response of rocks to a stress applied externally to the studied volume can take several idealised forms. For an ideal, linearly elastic material, the relationship between stress and strain follows a recoverable sloped linear trajectory, and the material resumes its initial geometrical state after the stress is removed (Figure 1A) (Jaeger et al., 2007). For an ideal plastic material, the relationship between stress and strain is initially similar to an elastic material, but at a certain shear stress threshold the plastic material undergoes 'yielding', after which the strain is non-recoverable (Jaeger et al., 2007). The strain vs. stress curve then becomes horizontal and defines a stable strength value (Figure 1A). Such idealised behaviours are widely used concepts for models of tectonic and magmatic crustal deformation (e.g. Scheibert et al., 2017; Vachon and Hieronymus, 2017).

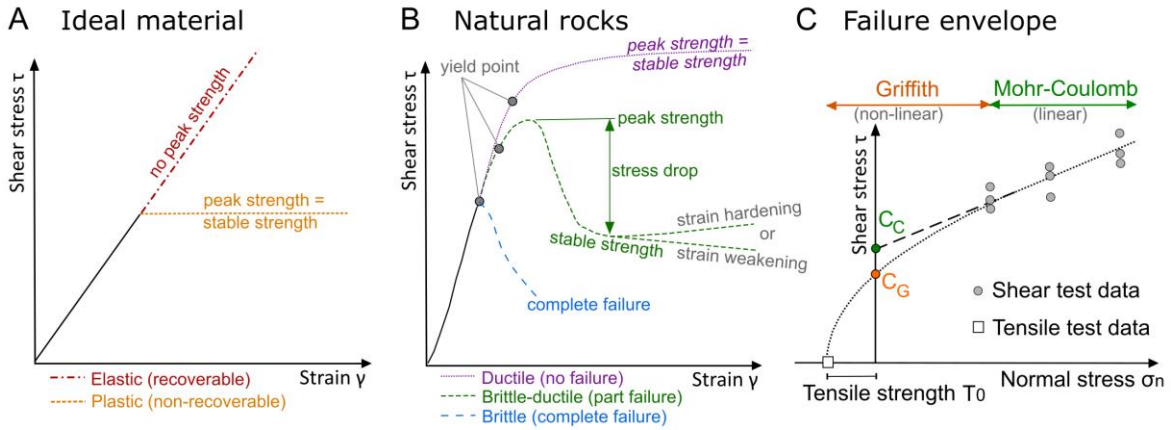


**Figure 1** – **A** Shear stress (τ) in an ideal Coulomb material that is subjected to an angular shear (γ) increases linearly until failure occurs and a constant peak strength is reached; **B** Shear stress in natural rocks under low confining stress increases until the yield point is reached after which either shear stress increases towards a stable strength in the ductile regime, or until a peak strength where failure occurs and shear stress again decreases towards a lower stable strength in the brittle-ductile regime (the difference is the stress drop), or after which shear stress decreases until complete failure in the brittle regime; **C** Shear test results from samples subjected to different confining normal loads ($\sigma_n$), combined with tensile strength ($T_0$) obtained from tensile tests together define the two-dimensional Mohr failure envelope of a material; the intercept with the vertical axis (τ) is the material's cohesion and can be estimated using e.g. a linear Coulomb ($C_C$) or non-linear Griffith ($C_G$) failure criterion (cfr. Jaeger et al. 2007).

Laboratory tests on natural rocks have shown a more complex behaviour (Byerlee, 1978; Jaeger et al., 2007). Upon or after 'yielding', a peak strength may be reached, after which the rock sample typically fails along a localised shear plane. The shear stress then decreases towards a lower, stable – or 'residual'– strength (Figure 1B, green). The difference between the peak strength and stable strength is the so-called stress drop. The stable strength may gradually increase or decrease at continued shearing, referred to as strain hardening or strain softening respectively (Figure 1B). Upon brittle failure, a sharp stress drop leads to an abrupt decrease in shear strength and – in the lab – can result in sample disintegration (Figure 1B, blue). Brittle failure is typical for low lithostatic pressures in the upper part of the crust (Paterson and Wong, 2005).

Ductile deformation, in contrast, is characterised by the absence of a stress drop (Figure 1B, purple), and it typically occurs at higher lithostatic pressures (i.e. at greater depths in the crust) (Byerlee, 1968; Jaeger et al., 2007; Schöpfer et al., 2013). Ductile materials can undergo strain hardening or softening and this deformation is non-recoverable as well. The brittle-ductile transition describes the level in the crust above which rock deformation is brittle, and below which it is ductile.

These insights of rock mechanics have been used for decades in laboratory – or analogue – experiments to study deformation processes in the Earth's crust, such as tectonic faulting (e.g. Dooley and Schreurs, 2012; Hubbert, 1937), seismo-tectonics (e.g. Reid, 1911; Rosenau et al., 2017), magma intrusion (e.g. Galland et al., 2018; Kavanagh et al., 2018b; Mastin and Pollard, 1988; Poppe et al., 2019) and gravitational collapse (e.g. Marti et al., 1994; Merle and Borgia, 1996). The selection of analogue materials is guided by the aim of obtaining physical similarity between the experiments and nature through dimensional analysis (Hubbert, 1937; Merle, 2015). Such considerations have favored the use of low-cohesive, frictional granular materials – dominantly sands (e.g. Cubas et al., 2013; Klinkmüller et al., 2016; Montanari et al., 2017; Roche et al., 2000; Schreurs et al., 2016, 2006), although another type of laboratory models use materials with simplified elastic or visco-elastic rheologies such as pigskin gelatin or laponite gel (e.g. Bertelsen et al., 2018; Kavanagh et al., 2018a; Rivalta et al., 2015 and references therein). Coulomb (1775) was the first to describe a linear relationship between normal load and shear stress at failure for granular media. Like rocks, sand is considered to deform largely according to a Mohr-Coulomb failure criterion (Figure 1C, green), with a realistic strain weakening behaviour controlling localisation of deformation into shear zones (Lohrmann et al., 2003; Ritter et al., 2016).

Studies using laboratory models traditionally focused on qualitative descriptions of structural geometries (e.g. Eisenstadt and Sims, 2005; Holohan et al., 2013; Roche et al., 2000). Recently, model deformation fields are routinely quantified by using advanced photogrammetry and image analysis techniques (e.g. Adam et al., 2005; Galland et al., 2016; Tortini et al., 2014) and most recently X-ray Computed Tomography (CT) (Adam et al., 2013; Holland et al., 2011; Kervyn et al., 2010; Poppe et al., 2019; Schreurs et al., 2003; Zwaan and Schreurs, 2017). Lately, such kinematic observations have been blended with both internal "in-situ" stress measurements (Moulas et al., 2019; Nieuwland et al., 2000; Seropian and Stix, 2018) and constraints on externally applied forces (Cruz et al., 2010; Cubas et al., 2013; Herbert et al., 2015; Ritter et al., 2018b, 2018a; Souloumiac et al., 2012) to derive a quantitative dynamic picture of faulting or other deformation processes in laboratory models.

Different emplacement techniques (sieving, pouring) yield sand packings of variable reproducibility, as demonstrated by mechanical tests (Lohrmann et al., 2003; Panien et al., 2006). Moreover, benchmarking experiments using different sands have demonstrated that variability in the granular characteristics (i.e. angularity, ellipticity) introduces uncertainties in quantified model outcomes (Schreurs et al. 2016). The evolution towards a more quantitative analysis of laboratory models requires quantified mechanical properties of granular analogues, the reduction of reproducibility uncertainty and better scaling of laboratory models to their natural prototypes (Gomes et al., 2006; Lohrmann et al., 2003; Montanari et al., 2017; Panien et al., 2006; Ritter et al., 2016).

Density, cohesion and friction coefficient are the three main parameters that have been used in dimensional analysis for scaling granular analogue materials; these properties can be obtained from a granular material by using mechanical tests, such as direct and ring shear tests (Abdelmalak et al., 2016; Galland et al., 2009; Merle, 2015; Montanari et al., 2017; Mourgues and Cobbold, 2003; Schellart, 2000; Zorn et al., 2020). Compared to sand – which is near-cohesionless –, more cohesive powders with finer grain sizes in the order of a few μm, such as silica flour, crushed (feldspar) sand, alumina powder, ignimbrite powder, kaolin clay, diatomite powder, powder sugar, wheat flour and gypsum powder, can be used purely or mixed as a filler into coarser-grained sand to represent more complex crustal deformation (e.g. Galland et al., 2018, 2006; Grosse et al., 2020; Mathieu et al., 2008; Montanari et al., 2017; Reber et al., 2020; Schellart and Strak, 2016 and references therein). These powders are able to form both tensile fractures and shear fractures, and they may follow a non-linear Griffith-Mohr-Coulomb failure criterion (Figure 1C, orange), instead of a linear Coulomb failure criterion (Figure 1C, green) (Abdelmalak et al., 2016; van Gent et al., 2010).

Abdelmalak et al. (2016) showed that, rather than relying on a single mechanical test, a combination of mechanical tests can make cohesion and friction coefficient tunable experimental variables for a range of mixtures of low-cohesion, low-friction with high-cohesion, high-friction granular materials of similar grain sizes.

As example of fine-grained filler in sand, hemihydrate gypsum powder (i.e. plaster) has been used in laboratory models of volcano-tectonic processes, such as magma intrusion, dome building or gravitationally-driven deformation (Byrne et al., 2015, 2013; Donnadieu et al., 2001; Holohan et al., 2008; Kervyn et al., 2010; Merle and Lénat, 2003; Poppe et al., 2019, 2015; Rincón et al., 2018; Roche et al., 2001; Zorn et al., 2020), and regional-tectonic processes, such as the evolution of normal fault zones in high-strength rocks (van Gent et al., 2010), near-surface gravitational instabilities, such as sinkhole collapse (Poppe et al., 2015) and landslides (Paguican et al., 2014; Shea and van Wyk de Vries, 2008). Apart from limited efforts (Donnadieu et al., 2001; Zorn et al., 2020), the physical and mechanical properties of sand-plaster mixtures have not been systematically investigated, however.

This study quantifies the mechanical behaviour of quartz sand mixed with gypsum powder at different weight ratios, by evaluating different mechanical testing methods. We first provide the context for the scaling of mechanical properties of analogue granular materials. We test the influence of the emplacement technique – pouring, sieving and compaction – on bulk density and estimate the material porosities. We also test the effect of ambient humidity. By using tensile tests, extensional tests, direct shear tests and ring shear tests, we constrain failure envelopes for each of the end-member sand and plaster materials and mixtures thereof. By assessing the goodness-of-fit of linear Coulomb versus parabolic Griffith failure criteria to the failure data, we then estimate the cohesions and friction coefficients. Our results enable a better understanding of modelling outcomes involving sand and plaster and their mixtures, and allow more realistic dynamic scaling of laboratory experiments using such materials.

## 2. Scaling of the mechanical properties of granular materials

The concept of scaling and dimensional analysis implies two successive steps: (1) identifying the dimensionless parameters that govern the modelled physical system, and (2) the geometrical, mechanical and dynamical equivalence – i.e. similarity – of laboratory models to their natural counterparts (Barenblatt, 2003; Gibbings, 2011; Hubbert, 1937). Abdelmalak et al. (2016), Merle (2015) and Reber et al. (2020) summarise how this equivalence can be reached for granular materials.

Dynamic similarity is classically discussed by assuming that a Coulomb failure criterion is representative of material failure in both model (*m*) and a natural prototype (*g*). The internal friction coefficient μ is a direct dimensionless parameter. Similarity implies that the friction coefficient must be equal in nature and in the laboratory:

(1) $\mu_m = \mu_g$

The cohesion C is combined with density ρ, gravitational acceleration g, and depth or length h (Hubbert, 1945; Merle, 2015) in the dimensionless parameter:

(2) $\prod = \frac{\rho \times g \times h}{C}$,

This parameter quantifies the balance between the gravitational forces and the cohesive forces; the system will be gravity-dominated if $\prod >> 1$ and cohesion-dominated if $\prod << 1$. Dynamic similarity of a laboratory model to a natural geological system is then usually reached by ensuring the friction coefficient of the model material matches that in nature. In addition, the model material cohesion $C_m$ required for a model that is subjected to the natural gravity field is calculated by rearranging equation (2):

(3) $C_m = \frac{C_g}{\rho_g \times h_g} \rho_m x\ h_m$,

Accordingly, the model cohesion dictates the length scale $h_g$ of the model with respect to the natural prototype. Different scales of observation, e.g. basin-scale vs. lithosphere scale, therefore necessitate different model cohesions (Abdelmalak et al., 2016). The length scale h* represents the dimensionless scale ratio between model and nature and equals $h_m/h_g$ (Table 1). In laboratory models of lithosphere-scale processes, one centimeter typically represents 10 km, translating into $l^* \approx 10^{-6}$ (e.g. Davy and Cobbold 1991), while in those of basin-scale processes, one centimeter most typically represents 100 to 1000 meters, translating into $l^* = 10^{-4}$-$10^{-5}$ (e.g. Dooley and Schreurs, 2012; Galland et al., 2018; Merle, 2015). Bulk densities of most natural crustal rocks range between 2200 and 3000 $kg.m^{-3}$, while analogue granular material bulk densities range between 1200 and 1800 $kg.m^{-3}$. This leads to model:nature density ratios ρ* of 0.4-0.8. Cohesions of natural rocks range broadly between $10^6$ and $10^8$ Pa (e.g. Galland et al., 2018; Schellart, 2000; Schultz, 1996; Voight and Elsworth, 1997).

For lithosphere-scale processes, ∏ values then range between 2 and 300, and so cohesions of model rocks should be considerably low, between 0.5 and 80 Pa. This is the case for pure silica sand (Klinkmüller et al., 2016; Schellart, 2000). For basin-scale or volcano-scale processes, ∏ values lie an order of magnitude lower, between 0.2 and 30, and cohesions of model materials should have a range between 40 and 800 Pa. Granular materials with higher

cohesion compared to sand are thus needed, by using fine-grained powders or fillers in coarse-grained sand.

**Table 1**: Scaling parameters and dimensionless equation used to compare experiments to nature; natural values from (Galland et al., 2014; Merle, 2015; Schultz, 1996).

| Parameter | Symbol and Unit | Model (m) | Nature(g) | Ratio* |
|---|---|---|---|---|
| Gravitational acceleration | g ($m.s^{-2}$) | ~9.81 | ~ 9.81 | ~1 |
| Overburden height | h (m) | $1x10^{-2}$ | $1x10^{1}$ –$15x10^{3}$ | $10^{-4}$-$10^{-6}$ |
| Density | ρ ($kg.m^{-3}$) | 1200-1800 | 2200-3000 | 0.4-0.8 |
| Cohesion | C (Pa) | 0.5-800 | $10^{6}$–$10^{8}$ | $10^{-4}$-$10^{-8}$ |
| Internal friction angle | Φ (°) = $\prod_3$ | 25-45 | 25–45 | ~1 |
| Internal friction coefficient | μ (radians) | 0.43-0.79 | 0.43-0.79 | ~1 |
| Gravitational stress:cohesion | $\prod = \rho gh/C$ | 0.2-300 | $0.015x10^{-4}$–$4x10^{3}$ | |

## 3. Materials and Methods

### 3.1 Materials

We tested mixtures of dry sand and plaster. The sand is 99,8% chemically pure silica sand MAM1ST-300 ($SiO_2$; Sibelco, Mol, Belgium). Scanning Electron Microscope (SEM) images, carried out at Vrije Universiteit Brussel, show that the grains are subangular to poorly rounded (Figure 2A). The grain size is unimodal, with a mean ~205 μm (Figure 2B). The plaster is air-dried hemi-hydrate gypsum powder with the brand name Goldband ($CaSO_4.1/2\ H_2O$; Knauf). SEM images show the grains are tabular to plate-shaped, and clustered (Figure 2C). Grain size measurements in water in a laser diffractometer without scintillation at Vrije Universiteit Brussel showed that the grain size distribution is unimodal, with a mean ~22 μm (Figure 2D), but this combines both 1-10 μm-sized individual crystals and 10-80 μm-sized clusters. The crystal hardness of quartz is 7 on the scale of Mohs, while that of gypsum crystals is 4.

The sand and plaster were mixed at 0, 5, 10, 20, 35, 50, 70 and 100 weight percent (wt%) of plaster. The quartz sand and gypsum plaster end-member materials and their mixtures are hereafter referred to as ‘samples’. Ambient air temperature was registered in all laboratory environments to be 18-25°C.

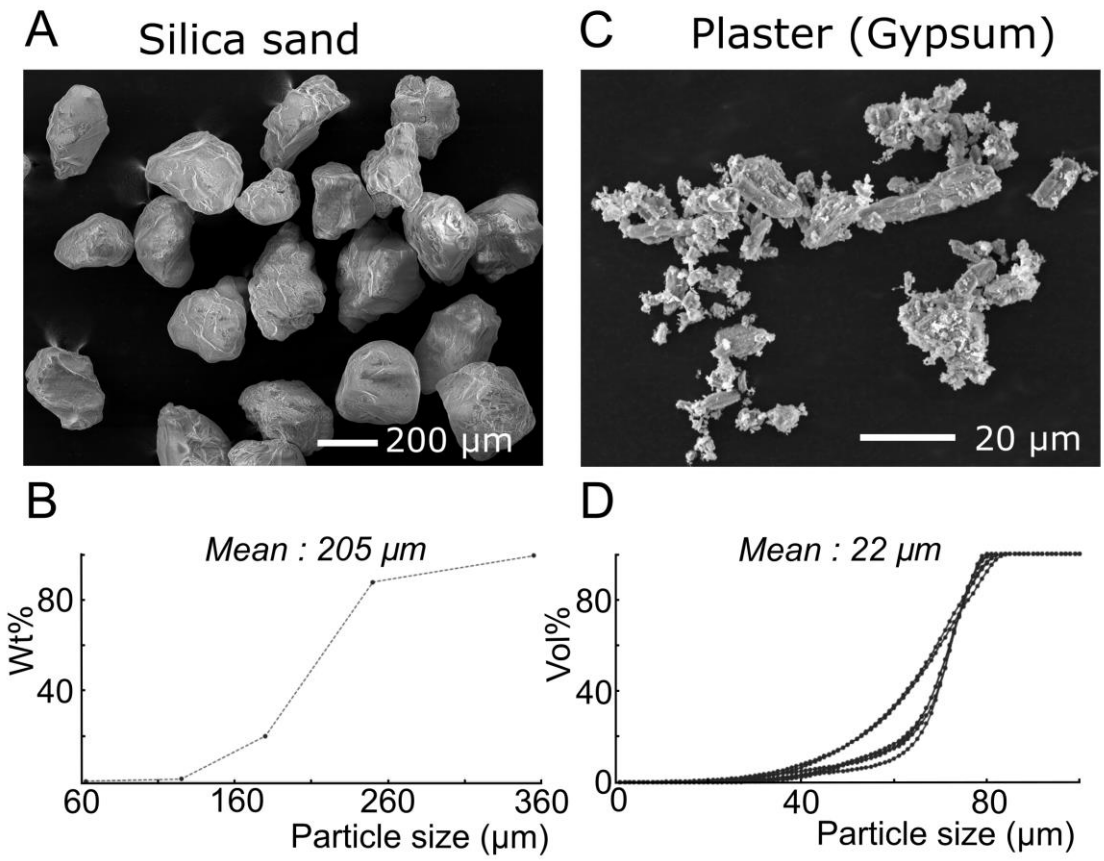


**Figure 2** – **A.** Scanning Electron Microscope (SEM) image of MAM1ST-300 silica sand grains shows moderately rounded grain shapes and a unimodal grain size; **B.** Cumulative particle size measurements show the silica sand used in this study has a mean particle size of 205 µm (Sibelco); **C.** SEM image of Knauf gypsum powder – i.e. plaster - used in this study shows micrometer-sized, tabular and blocky crystals often in clusters of several tens of µm; **D.** Cumulative particle size measurements show that the mean plaster particle size is about 22 µm but clusters sizes are up to 80 µm.

## 3.2 Methods

### *3.2.1 Bulk density estimates and effects of emplacement method*

The effects of three emplacement methods were assessed: (1) pouring, (2) sieving versus, and (3) pouring and compaction. The first two methods were assessed by systematically measuring the bulk density ρ of sand-plaster mixtures with 0, 10, 20, 50 or 100 wt%. plaster in ring shear tests (see Section 3.2.3). The air-dried granular materials were placed into a ring-shaped shear cell, which is 4 cm high, $1.10^{-3}$ m³ (1 liter) in volume and of a mass of 2186.5 g, either by sieving through a 400 µm mesh, or by pouring from an open pitcher. The samples were emplaced from ~20 cm height, which was previously found to be the most efficient height for obtaining a most compact quartz sand packing (Lohrmann et al., 2003). Surplus

material was scraped off the cell top manually and the emplaced sample mass was then obtained by weighing the filled test cell on a balance.

The third emplacement method, and the effects of humidity, were examined through a second set of identical mixtures that were oven-dried for 24 hours, poured in the shear cell from ~20 cm height and compacted by preloading with a normal load of 20000 Pa on the ring shear tester. The ring shear test procedure includes the estimation of material density before and during the test, which provided a means of assessing the effect of material compaction during deformation (see Section 3.2.3).

### *3.2.2 Porosity estimates*

The bulk porosity φ of each granular material was estimated through the equation:

(4) $\varphi = (V_s - (((M_s.F_q)/\rho_q) + ((M_s.F_p)/\rho_p)))/ V_s$

Here, $F_q$ and $F_p$ are the known bulk fractions of quartz sand and gypsum powder, respectively. $V_s$ is the sample bulk volume and $M_s$ is the sample bulk mass. The individual crystal density of quartz $\rho_q$ is taken to be 2655 $kg.m^{-3}$ and that of hemihydrate gypsum $\rho_p$ is taken to be 2730 $kg.m^{-3}$ (van Gent et al., 2010).

### *3.2.3 Ring shear tests*

We generally followed the ring shear test protocol for measuring internal friction with the RST01.pc as described in Klinkmüller et al. (2016). The shear cell containing the sample was placed on the ring shear tester (Figure 3A) and the lid was lowered into the sample surface. A normal load was then applied by the lid to the air-dried poured or sieved sample under rest, that varied in separate test runs from 500, 1,000, 5,000, 10,000, 15,000 to 20,000 Pa. For comparison with direct shear test data, oven-dried samples were poured and then compacted in the ring shear cell by pre-loading with a normal load of 20,000 Pa for 5 seconds. Then, the normal load was returned to respectively 250, 500, 1,000, 2,000 or 5,000 Pa in separate test runs.

The cell was then rotated clockwise at a constant angular velocity of $4.4°.min^{-1}$, or 6 $mm.min^{-1}$ (with respect to the median line of the sample-contained ring of the shear cell) during 300 seconds (or 30 mm of shear). A set of 5-mm deep, vertical radial blades on the lid caused localisation of shear inside the sample material and prevented shear at the interface between the sample and the cell lid. During the test all signals from sensors (normal and shear load, lid position and velocity) were recorded at 100 Hz and then down-sampled to 10 Hz to smooth high-frequency noise.

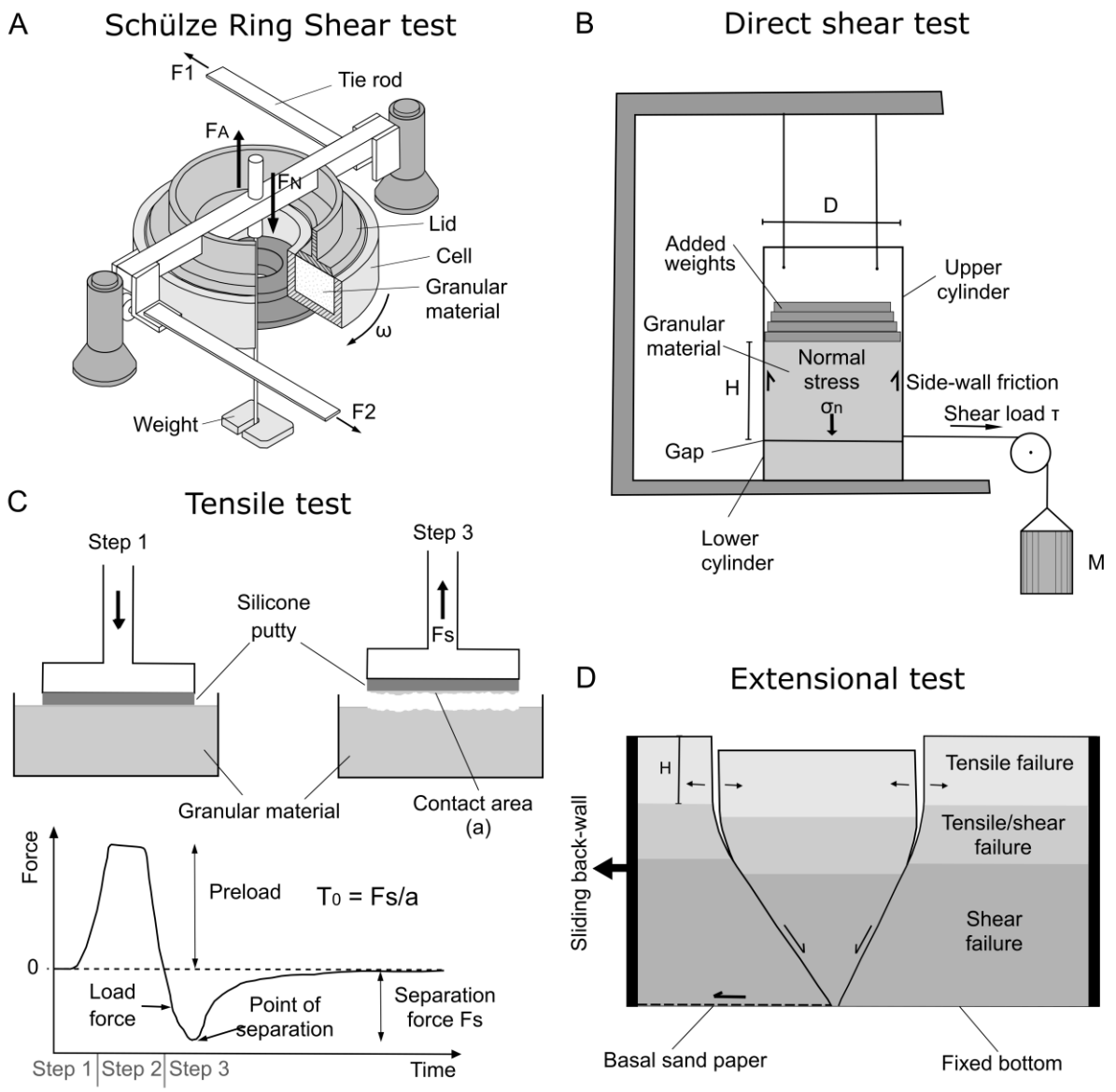


**Figure 3** – Laboratory set-ups used for testing the physical properties of granular materials. **A.** Schülze ring shear tester (RST). The sample is placed in an annular cell and on top of the sample a lid is suspended to which a normal load is applied. During a test run the sample-bearing cell is rotated and tie rods measure the shear stress (F1, F2) undergone by the lid. **B.** Hubert-type direct shear tester apparatus, in which a sample is placed in a cylinder consisting of an upper half suspended above a stable lower half. A shear load M is applied to the upper cylinder and is incrementally increased until sample failure occurs. Tests are repeated with constant sample height H but increasing normal loads by adding weights. **C.** Tensile test where the tensile strength of a compacted granular sample is obtained through a 3-step procedure in which a silicone pad is preloaded on the top of a granular sample and subsequently retracted until sample failure occurs at a measured separation force. **D.** Extensional test in which a compacted granular sample is extended horizontally until failure occurs by retracting a moving wall. The height H of the vertical upper part in the tensile failure domain of the induced fractures is a measure for the tensile strength of the material.

The registered shear stress curve is typical for granular materials (Figure 1B, green) and consists of three parts (Lohrmann et al., 2003; Panien et al., 2006): (1) a peak shear strength (i.e. static failure) that is reached shortly after test initiation, (2) a stress drop then reflects localisation of shear into a shear zone; (3) a stable plateau is reached representing the steady state stable shear strength; (4) after a short reversal of shear cell rotation direction to return shear stress to zero, shearing anew in a clockwise direction returns the shear curve to a dynamic shear strength which represents shear zone reactivation.

For each normal load, tests were repeated three times, amounting to 18 tests for each material in total. Peak shear strengths were picked manually or automatically (Rudolf and Warsitzka, 2019; Warsitzka et al., 2019). Stable and dynamic shear strengths are not discussed further here, but they are available in the accompanying data publication (Poppe et al., 2021).

During shearing, vertical lid movement is measured as a proxy for sample decompaction (positive) or compaction (negative). This measurement allowed us to study the effect of sample decompaction/compaction, and thus density variations, on sample frictional properties.

An additional velocity stepping test was carried out on a 90 wt% sand – 10 wt% plaster mixture to assess the dependency of measured shear strengths on the shear rate, by decreasing the shear rate after reaching the steady state plateau incrementally from 5 $mm.s^{-1}$ to 2.5, 1, 0.5, 0.1 and 0.05 $mm.min^{-1}$.

### *3.2.4 Humidity tests*

To estimate the humidity content, one air-dried sample of a mass of ~400g of each sand, plaster, and sand-plaster mixtures containing 5, 10, 20, 35, 50 and 70 wt% plaster, all stored previously in their original packaging at room temperature and ambient air humidity, were weighed on a precision balance (precision = 0.01g). Then, the samples were placed in open containers in an oven at a temperature of 90°C and weighed again after 24, 48 and 72 hours of oven-drying. The drying process evaporated the sample's moisture, and the loss of sample mass yielded a weight percentage (wt%) of humidity loss. Furthermore, to constrain the effect of humidity on the mechanical properties of 100 wt% plaster, we carried out direct shear tests, tensile and extensional tests both on oven-dried plaster and on air-dried plaster.

### *3.2.5 Direct shear tests*

Pressures of <500 Pa are typical in sand-box experiments with a few centimeters of material height (depending on material density - cf. equation 2). Because standard ring shear tests at

normal loads of < 500 Pa are possibly subject to bias (Ritter et al., 2016), we performed Hubert-type direct shear tests at normal loads of ~100 to ~1200 Pa. The Hubert-type shear apparatus consisted of an upper PVC cylinder suspended above a fixed lower PVC cylinder, with a cardboard ring maintaining a gap of < 1 mm in between both cylinders (Figure 3B).

To avoid humidity effects on material properties, samples were first oven-dried at 90°C for at least 24 hours, left to cool in a sealed container, weighed on a precision balance and poured in the cylinders of the shear apparatus. A lid was placed on top of the sample, and by manual tapping from above on the lid, the sample was compacted down until a height H of 2.5 cm above the gap between both cylinders to obtain the density pre-determined for that material ($\rho_{Compacted}$ in Table 2). The mass of material within the upper cylinder under gravity represented an initial normal load on the horizontal plane passing between the cylinders. Up to four weights could be added on top of the sample, to give a range of five normal loads. The normal stress $\sigma_n$ acting on the horizontal plane between the cylinders is obtained by dividing normal load by the circular area of the plane. After sample emplacement, compaction and vertical loading, the cardboard ring between both cylinders was carefully removed without disturbing the sample. To obtain the shear strength $\tau$, a shear load was applied to the upper cylinder by pouring sand in a small container connected to the cylinder via a pully (Figure 3B). This load was increased until an initial sample failure was detected by visual inspection at the gap between both cylinders. The applied mass M causing shear failure was then constrained by weighing. From this, the gravitational acceleration g, and the circular shear plane area A (i.e. cylinder section), the sample's shear strength (i.e. the critical shear stress acting on the shear plane) was calculated according to the equation:

(5) $\tau = gM/A$

This test was repeated three times for each of the five normal loads to ensure minimum reproducibility. Thus, a total of 15 measurements were made for each mixture and end-member granular material. In cases where the range of the obtained measurement values was large, additional runs were carried out. The average shear strength value at each normal load was used to construct failure envelopes in shear stress $\sigma_s$ vs. normal stress $\sigma_n$ diagrams, following correction of the normal stress for the so-called silo effect.

The 'silo effect' or 'Janssen effect' is a reduction in the normal load on the shear plane due to friction on the wall of the upper cylinder (Jansen, 1895; Mourgues and Cobbold, 2003). This can be corrected empirically. The upper cylinder of the Hubbert-type shear apparatus was suspended above a precision balance. A cardboard ring maintained a gap of <1 mm between the cylinder and the balance. A sample was then poured and compacted in the suspended

cylinder to obtain the same densities as used in the direct shear tests (Table 2). The cardboard ring was then removed. The mass then registered by the balance was the effective normal load exerted on the failure plane in the direct shear tests. These normal load measurements were repeated at least three times for each of the five normal loads in the direct shear tests, and the average 'corrected normal load' was used instead of the theoretical normal load to construct failure envelopes.

### *3.2.6 Tensile tests*

The tensile strength $T_0$ of oven-dried sand, plaster and sand-plaster mixtures containing 5, 10, 20, 35, 50 and 70 wt% plaster, and air-dried plaster was measured at the University of Maine, France, following the method of Schweiger and Zimmerman (1999). Each material was poured into a container of 108 $cm^3$ in volume and with a square-shaped area of 6x6 $cm^2$. It was then compacted by manually tapping a cover from above to obtain the required density (Figure 3B). A pad of the silicone polymer polydimethylsiloxane (PDMS) with a viscosity of ~$10^4$ Pa.s (Poppe et al., 2019) was attached to the bottom of a square-shaped load cell measuring 4x4 $cm^2$, which was mounted on an EZ-SX tension apparatus.

The tensile strength test consisted of three steps (Figure 3C). In step 1, the sample was vertically preloaded by the load cell for five seconds to allow the silicone to adhere to the sample surface. In step 2, the loading was reduced until the tension force sensor measured 0 N. In step 3, an increasing vertical tensional force was exerted on the granular material by moving the silicone pad upwards at a constant displacement rate until a peak tension force $F_t$ was reached at failure. A photograph of the post-test silicone pad was referenced in ArcGIS software (ESRI). Here, the area of separated granular material $A_s$ was traced and quantified. The tensile strength $T_0$ was then obtained through the equation:

(6) $T_0 = F_t/A_s$

Tensile strength tests were reproduced ten times for the sand and plaster end-members and each sand-plaster mixture.

### *3.2.7 Extension tests*

On the assumption that the failure envelope of a material is non-linear at negative normal loads and at small positive normal loads, the cohesion of granular materials can be estimated by combining the tensile strength $T_0$ with a vertical cliff height H obtained from extensional tests (Abdelmalak et al., 2016). H was measured at the Vrije Universiteit Brussel, Belgium, in an extensional apparatus that consists of a box with three fixed glass walls and one moving

wall connected to a computer-controlled piston (Figure 3D). Attached to the moving wall was sandpaper that covered half of the box bottom length.

A weighed amount of oven-dried sand, plaster or sand-plaster mixtures containing 5, 10, 20, 35, 50 and 70 wt% plaster, or air-dried plaster was poured in the box. Sample compaction to a vertical height of 10 cm and the required density (see Table 2) was obtained by manual tapping on a lid from above. By moving the wall laterally outwards at a constant rate of 10 cm/hr, the attached sandpaper imposed a velocity discontinuity to the base of the sample pack, which extended until two or more fractures developed, forming a graben-like structure. At and just below the surface, each fracture is vertical and opening mode in the tensile failure domain; with depth the fracture becomes inclined and transitions to shear mode in the shear failure domain (Figure 3D). We measured the height H of the opening-mode shallow part of the fractures.

## 4. Results

### 4.1 Effects of emplacement method

We observed clear effects of the method of emplacement of sand-plaster mixtures – i.e. sieving, pouring or pouring + compaction – on the heterogeneity, density and porosity of the sample material.

#### *4.1.1 Material heterogeneity*

The dispersal of grainsize of a sand-plaster mixture, and thus of mineralogy, is strongly affected by the emplacement method. Pouring a mixture quasi-instantaneously maintained a homogeneous sand and plaster distribution (Figure 4A and Table 2). Sieving the mixture, however, resulted in heterogeneous grain-size and mineralogical distribution as the sand and plaster separated into thin layers (Figure 4A).

#### *4.1.2 Material density*

The pre-test bulk densities show systematic variation depending on the emplacement method and sand-plaster mixing ratios (Figure 4B; Table 2). Firstly, the mean density of quartz sand is significantly higher when sieved (1410 ± 5 kg $m^{-3}$) than poured (1235 ± 7 kg $m^{-3}$) ($\alpha$ = 0.050; p = 1.69 x $10^{-25}$; t-statistic = -127.61; t-critical = 2.12), whereas the density of plaster is significantly lower when sieved (564 ± 6 kg $m^{-3}$) than poured (636 ± 11 kg $m^{-3}$) ($\alpha$ = 0.050; p = 4.40x$10^{-13}$; t-statistic = 21.03; t-critical = 2.12). At a 50:50 wt% sand:plaster ratio, the

density of sieved (899 ± 7 kg $m^{-3}$) and poured (906 ± 9 kg $m^{-3}$) samples is not significantly different ($\alpha = 0.050$; $p = 6.67x10^{-2}$; t-statistic = 1.97; t-critical = 2.12).

Secondly, pouring+compaction produced higher bulk densities than either sieving or pouring. Compaction increased the bulk density of plaster to 900 kg $m^{-3}$ regardless of whether done by pre-loading (RST) or tapping (DST). Compaction by tapping more effectively increased the bulk density for sand-rich mixtures (i.e. <35 wt% plaster) and produced a bulk density of 1700 kg $m^{-3}$ for the sand end-member; this is approximately double that of plaster (Figure 4B; Table 2).

Thirdly, whether poured, sieved or poured+compacted, the bulk density of a sand-plaster mixture systematically decreases with increased plaster content. This decrease is not linear – bulk density decreases more rapidly for both the poured and the poured+compacted samples after about 20 - 35 wt% plaster.

#### *4.1.3 Material porosity*

The estimated bulk porosity of the samples relates inversely to the bulk density (Figure 4C; Table 2). Depending on the emplacement technique, the inferred porosity of quartz sand was varied between 36-54 vol%, whereas that of plaster varied between 67-78 vol%. In mixtures of these end-members, the porosity increased systematically, but non-linearly, with increasing plaster content by weight.

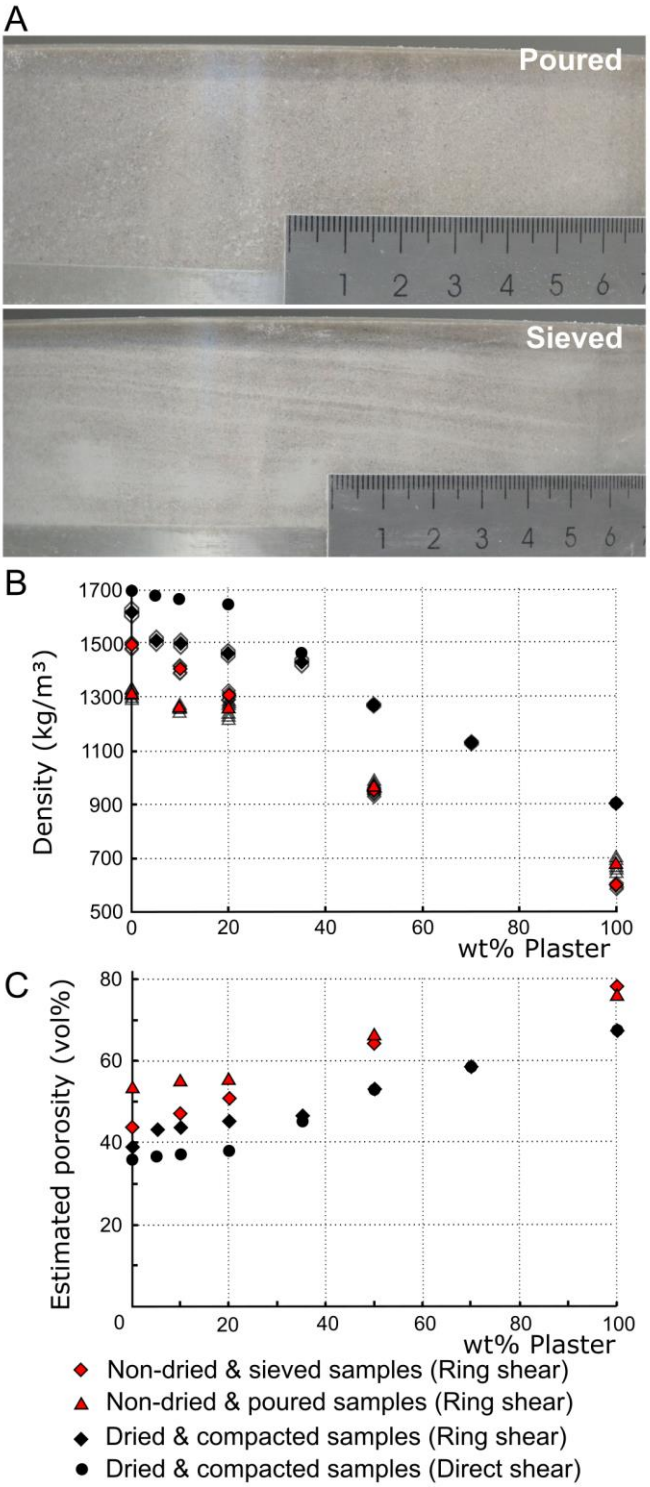


**Figure 4** – Effect of the emplacement technique on sand-plaster mixtures. **A.** Homogeneous grain size distribution in a poured 90-10 wt% sand-plaster sample vs. heterogeneous grain size distribution in a sieved 90-10 wt% sand-plaster sample with alternating coarser (sand-dominated) and finer (plaster-dominated) grain size layers; **B.** Densities of non-dried samples emplaced by pouring or sieving, or oven-dried samples poured and compacted into the ring shear cell, and oven-dried poured and compacted samples in direct shear tests, tensile tests and extension tests. The filled symbols indicate averages of the light-grey individual measurements. **C.** Inferred porosities of poured, sieved and poured+compacted samples.

**Table 2** – Density, porosity and humidity of sand and plaster and their mixtures in function of the method of emplacement described in Section 3 and Figure 4B-C; sieved and poured samples were air-dried, poured+compacted samples were oven-dried; ρ = density; φ = porosity; uncertainties on sieved and poured densities are standard deviations (1σ), uncertainties on humidity indicate measurement precision relative to the total sample weight.

| Sand:Plaster ratio (wt%) | Plaster (wt%) | $\rho_{Sieved}$ (kg.m$^{-3}$) | $\rho_{Poured}$ (kg.m$^{-3}$) | $\rho_{Compacted}$ (kg.m$^{-3}$) | $\rho_{Compacted\ ring\ shear}$ (kg.m$^{-3}$) | $\varphi_{Sieved}$ (vol%) | $\varphi_{Poured}$ (vol%) | $\varphi_{Compacted}$ (vol%) | $\varphi_{Compacted\ ring\ shear}$ (vol%) | Humidity Weight loss (wt%) |
|---|---|---|---|---|---|---|---|---|---|---|
| 100:0 (Sand) | 0 | 1410±5 | 1235±7 | 1700 | 1625±26 | 43.6 | 53.5 | 36.0 | 38.8 | 0.05±0.03 |
| 95:05 | 5 | - | - | 1680 | 1514±18 | - | - | 36.8 | 43.0 | 0.17±0.03 |
| 90:10 | 10 | 1327±6 | 1190±4 | 1666 | 1505±17 | 47.1 | 55.3 | 37.4 | 43.5 | 0.29±0.03 |
| 80:20 | 20 | 1237±8 | 1187±14 | 1650 | 1467±11 | 50.9 | 55.5 | 38.2 | 45.0 | 0.28±0.03 |
| 65:35 | 35 | - | - | 1465 | 1439±18 | - | - | 45.4 | 46.3 | 0.38±0.03 |
| 50:50 | 50 | 899±7 | 906±9 | 1268 | 1272±8 | 64.6 | 66.4 | 52.9 | 52.8 | 0.79±0.03 |
| 30:70 | 70 | - | - | 1125 | 1133±10 | - | - | 58.4 | 58.2 | 0.76±0.03 |
| 0:100 (Plaster) | 100 | - | - | 900 | 901±2 | 78.1 | 76.7 | 67.0 | 67.0 | 1.03±0.03 |
| 0:100 (non-dried plaster) | 100 | 564±6 | 636±11 | 900 | - | - | - | 67.0 | - | - |

## 4.2 Humidity tests

After 72 hours of oven-drying at 90°C, samples showed a cumulative weight loss that increased roughly linearly ($R^2$ = 0.93) with increasing plaster content (Figure 5; Table 2). While plaster lost a cumulative 1.05 wt% of moisture, quartz sand only lost 0.05 wt%. For all samples, more than 90% of the weight loss occurred in the first 24 hours of oven-drying (see data in Poppe et al., 2021), suggesting that drying overnight should be sufficient to remove most of the humidity from granular materials prior to experimentation.

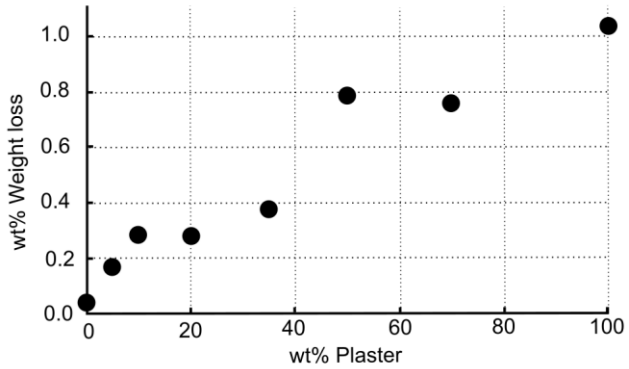


**Figure 5 -** Weight loss of sand-plaster mixtures of varying weight ratios after 72 hours of oven drying as a proxy for humidity contained within one sample per material.

## 4.3 Ring shear tests

### *4.3.1 Effect of shear rate*

The shear stress in a 90:10 wt% air-dried sand-plaster mixture measured at a shear rate of 2.5 $mm.min^{-1}$ increased by 2% compared to that measured at 25 $mm.min^{-1}$ (see data in Poppe et al., 2021). This observation indicates a weak dependency of the measured shear stress on shear rate. While we consider this effect quantitatively marginal compared to reported error margins, one may scale the friction coefficients reported here to the actual shear rate used or observed in experiments by a correction factor of 2% per order of magnitude deviation from the 6 $mm.min^{-1}$ used in our ring shear tests.

### *4.3.2 Stress and dilation curves for air-dried uncompacted samples*

We performed 300 individual ring shear tests on poured or sieved, air-dried sand, plaster and sand-plaster mixtures with 10, 20 and 50 wt% plaster, and on oven-dried, poured+compacted sand, plaster and mixtures with 5, 10, 20, 35, 50 and 70 wt% plaster (see data in Poppe et al., 2021).

The shear stress and compaction curves for air-dried sieved or poured sand samples describe the effect of the emplacement technique on the mechanical behaviour of sand-plaster mixtures (Figure 6). Note that negative dilation by convention represents compaction (Lohrmann et al., 2003).

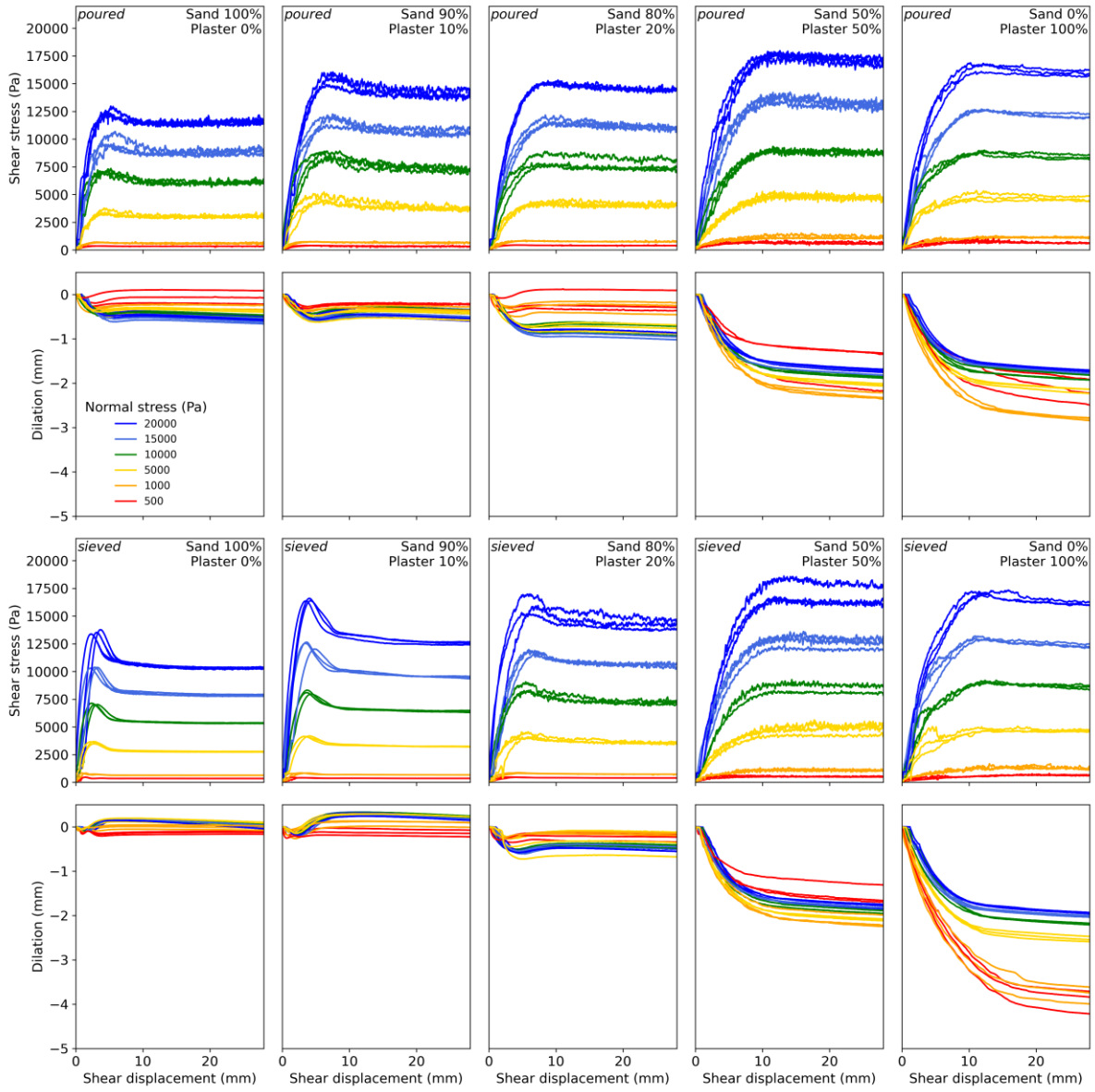


**Figure 6 – A.** Shear stress (τ) and sample dilation evolution as a function of time for air-dry poured versus sieved sand and plaster and 90:10, 80:20 and 50:50 mixing ratios. Ring shear test data (RST) at normal loads ranging between 500 Pa and 20,000 Pa at constant shear rate. Sample dilation is measured as RST lid uplift during shearing. Negative is compaction, positive is decompaction.

For sieved pure sand, shear stress and compaction evolution are qualitatively similar to what was observed previously for other silica sands (Klinkmüller et al., 2016; Lohrmann et al., 2003; Panien et al., 2006). After an initial phase of compaction during shear stress build-up, decompaction accompanies shear zone localisation and failure occurs at a peak shear strength value concurrent with the maximum decompaction rate. The measured shear stress then drops to a dynamic plateau value without further decompaction. Overall, the peak strengths and post-peak plateau strengths increase with increased normal loads.

As the plaster content increases in sieved samples, three alterations to this well-established shearing behaviour are seen (Figure 6, bottom rows). Firstly, the initial peak is wider; i.e. more strain is needed to localise a shear zone. Secondly, the associated stress drop gradually decreases, and a peak is absent from a 50:50 sand-plaster ratio onwards; i.e. the behaviour of plaster-dominated mixtures is more ductile. Additionally, the stable sliding strength at a given normal load generally increases with increased plaster content. Thirdly, the compaction-decompaction cycle observable in sand-dominated mixtures (≤ 20 wt% plaster) is replaced by steady compaction during localisation in the plaster-dominated mixtures (≥ 50 wt% plaster).

For poured samples, the temporal evolution of shear stress and decompaction is qualitatively similar to what has been observed for sieved samples (Figure 6, top rows). Nonetheless, there are some quantitative deviations. First, the peaks are generally wider (i.e. localisation requires more strain) and stress drops are smaller when poured compared to when sieved. Second, high-frequency noise indicates stick-slip, except for pure sand, and such noise is typically higher in amplitude compared to sieved samples. In sand-dominated samples, a clear initial peak with stress drop occurs again, although it is accompanied by a more subtle compaction-decompaction cycle (without net decompaction). In plaster-dominated poured mixtures, such a peak stress is again absent and is replaced by strain strengthening and sample compaction until the dynamic steady state is reached.

### *4.3.3 Stress and dilation curves for oven-dried compacted samples*

Figure 7 depicts the ring shear test results and dilation curves obtained for oven-dried sand, plaster and sand-plaster mixtures that were poured and mechanically compacted prior to testing. In general, the shear stress curves for these poured and pre-compacted samples are not as noisy as those for their poured and uncompacted equivalents (see Figure 6).

For sand-dominated mixtures (≤ 35 wt% plaster), initial shear stress peaks are again present at all tested normal stresses. These materials thus display a similar strain hardening to strain

weakening behaviour, accompanied by compaction-decompaction cycles, as seen in the above tests on air-dried samples and as described by (Panien et al., 2006).

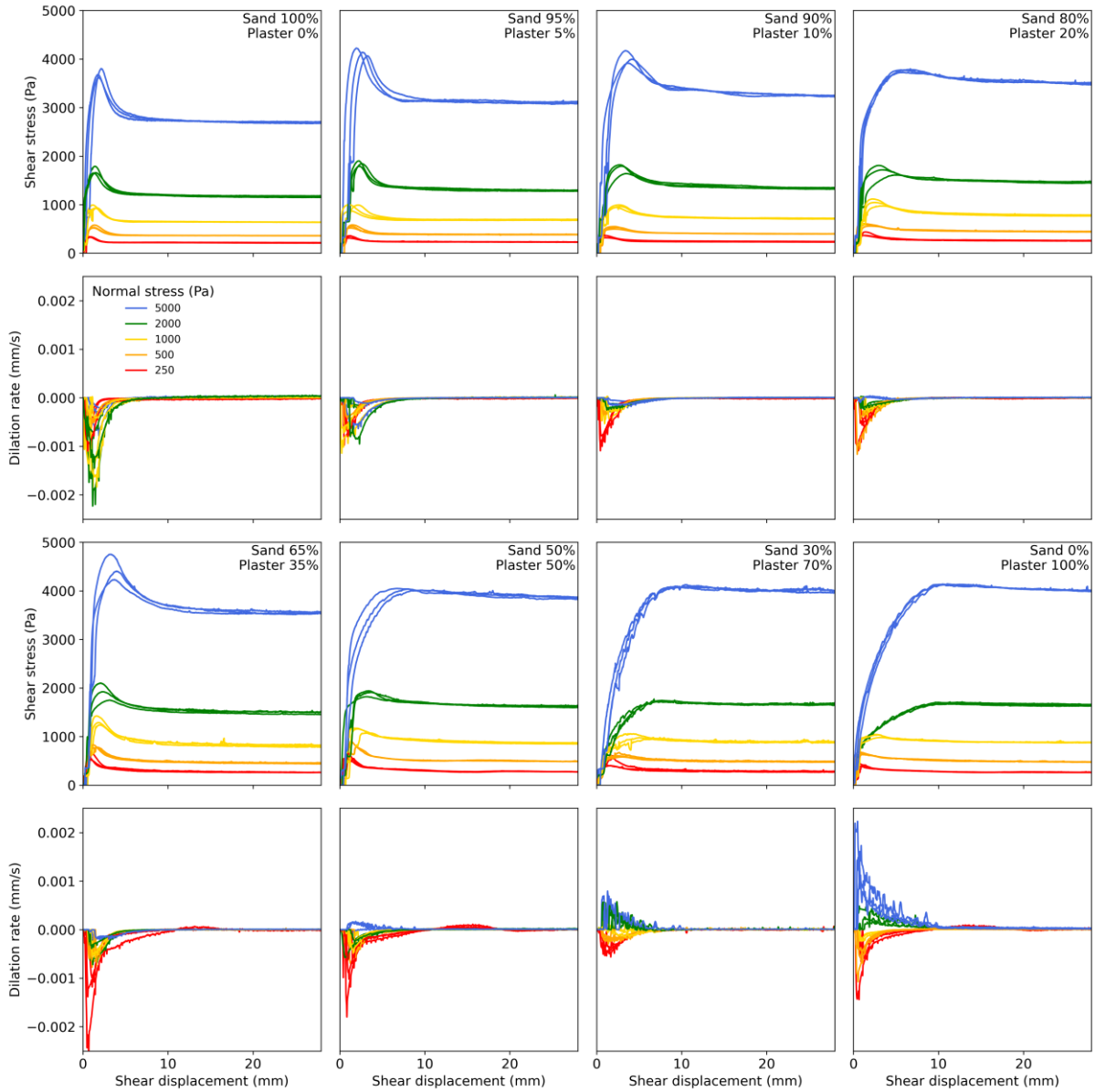


**Figure 7:** Curves of shear stress versus shear displacement and of dilation rate for oven-dried, poured+compacted sand, plaster and sand-plaster mixtures measured by using ring shear tests (n=120). Applied normal stresses varied from 250 to 5000 Pa.

For plaster-dominated mixtures (≥ 50 wt% plaster), a peak stress and compaction-decompaction behaviour is also seen at low normal loads. This is more brittle behaviour than the generally ductile behaviour seen in equivalent mixtures that were uncompacted prior to testing (see Figure 5). In addition, stick-slip behaviour is apparent in the stress-displacement curves at intermediate to high normal loads (>1000 Pa). At high normal loads, the pre-compacted plaster-dominated mixtures nonetheless again show pure strain hardening behaviour without a stress drop and with compaction only (i.e. ductile behaviour). The

583 transition from somewhat brittle behaviour to entirely ductile behaviour occurs at decreasing
584 normal stresses for increasing plaster contents. For a 50:50 wt% sand-plaster mixture, the
585 transition lies between 2000-5000 Pa; for a 30:70 wt% mixture it lies between 1000-2000 Pa;
586 for pure plaster it lies between 500-1000 Pa.
587
588 ***4.3.4 Peak stress data from ring shear tests***
589 Peak stress generally increases with increased normal load for all materials regardless of
590 emplacement procedure (Figure 8). The variation of peak strength with plaster content and
591 emplacement technique is more complex, however.
592 For air-dried uncompacted samples, peak shear stresses for a given normal load generally
593 increase with increased plaster content (Figure 8, red symbols). For sand-dominated sieved
594 mixtures (Figure 8, red diamonds), peak shear stresses are higher than for sand-dominated
595 poured mixtures (Figure 8, red triangles). For plaster-dominated sieved mixtures, on the other
596 hand, peak shear stresses are lower than for plaster-dominated poured mixtures.
597 For oven-dried and compacted samples, a general increase in peak stress for a given normal
598 load is not so clear (Figure 8, black diamonds). Rather, values generally increase up to 50
599 wt% plaster, the peak stresses are similar for compacted and uncompacted samples. For pure
600 plaster, however, the peak shear stress values of compacted samples are lower than those of
601 non-compacted samples.

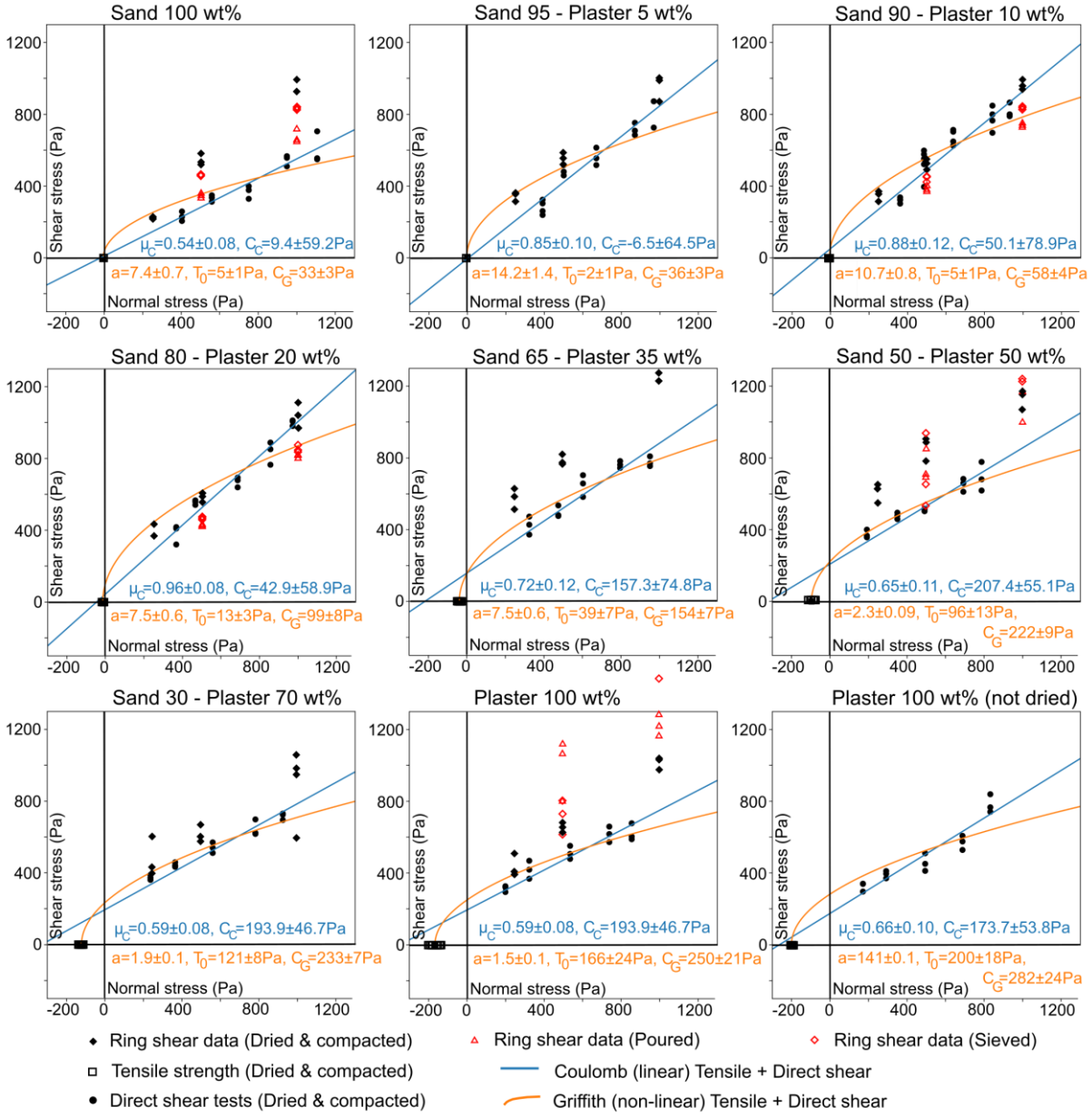


**Figure 8** – Shear stress ($\tau$) versus normal stress ($\sigma_n$) plots describing failure envelopes of oven-dried and compacted sand and plaster and their mixtures, composed of tensile strengths ($T_0$) obtained from tensile tests, direct shear test results (with normal loads corrected for the silo effect, see Supplementary Materials) and ring shear test results. Note that ring shear test data on sieved and poured samples were done on non-dried samples in equilibrium with ambient air humidity. Optimal failure envelopes shown here are based on fitting a Coulomb criterion (blue lines) or a Griffith criterion (orange curves) to direct shear and tensile test data on the oven-dried and poured+compacted samples.

### 4.4 Direct shear tests

We performed 143 direct shear tests on oven-dried poured+compacted sand, plaster and sand-plaster mixtures and on air-dried poured+compacted plaster (Figure 8).

#### *4.4.1 Correction for the silo effect*

The results of the empirical correction for the 'silo effect' (Jansen, 1895; Mourgues and Cobbold, 2003) are shown in Supplementary Figure S1 and raw data in Poppe et al. (2021). The tested range of normal stresses overlaps with that of the three lowest normal load steps in the ring shear tests (250, 500 and 1000 Pa). The measured normal stress versus applied normal stress curves deviate from a 45° slope. This deviation is greatest for mixtures with 35 and 50 wt% plaster. Therefore side-wall friction decreases the applied normal stress at the shear failure plane in all samples, and these curves enable a correction to obtain the average effective normal stress on the failure plane that was used to plot direct shear test data in Figure 8.

#### *4.4.2 Shear strength of oven-dried and compacted samples*

The direct shear test results – i.e. shear strength values versus normal stress values that are corrected for the side-wall friction effect – are displayed in Figure 8 (black circles). For all mixtures, the shear strengths from the direct shear tests are lower than the peak strengths from the ring shear test results on oven-dried and poured+compacted samples, except for mixtures with 10 and 20 wt% plaster, where they are broadly similar for similar normal stresses. Overall, the direct shear test results describe approximately linear failure envelopes in shear – normal stress space. There is a general increase in shear strength at a given normal load as plaster content increases to about 20 wt%. With higher plaster contents, however, the shear strengths at the tested normal loads remain slightly higher than those of pure sand.

### 4.5 Tensile tests

We performed 89 unconfined tensile tests on oven-dried and compacted sand, plaster and sand-plaster mixtures (Figure 9A; Table 3). Sand-plaster mixtures with < 20 wt% plaster display average tensile strengths that are near-zero (2-5 Pa) with little to no data spread. From 20 wt% plaster upwards, the tensile strength increases with plaster content along a roughly linear trend ($R^2 = 0.969$), up to a mean value 167 ± 23 Pa for pure, oven-dried plaster. The data spread increases with increasing plaster content in a mixture. Non-dried plaster yields a tensile strength of 200 ± 18 Pa, the mean of which is ~33 Pa. This is almost 20% higher than, and statistically distinct from, the mean tensile strength value of oven-dried plaster ($\alpha$=0.050; p=0.004; t-statistic=4.00, t-critical=2.31).

### 4.6 Extension tests

We performed 25 extensional tests on oven-dried and compacted sand, plaster and sand-plaster mixtures, in which a total of 73 vertical opening-mode fracture portions were measured (Figure 9B; Table 3). Quartz sand extended in a diffuse manner and developed unmeasurably low cliffs. An arbitrary value of 0.1 cm, representing measurement limit, was therefore assigned here to pure sand.

From 10 wt% plaster upwards, open fractures were observed. With increasing plaster content, the height of the opening-mode fractures increases roughly linearly ($R^2 = 0.899$). The material is able to develop opening-mode fractures to greater depths.

Non-dried plaster yielded vertical fracture heights that were on average 1.2 cm higher compared to oven-dried plaster. Despite their ranges overlapping, these averages are statistically distinct ($\alpha$=0.050; p=0.046; t-statistic=2.36, t-critical=2.31).

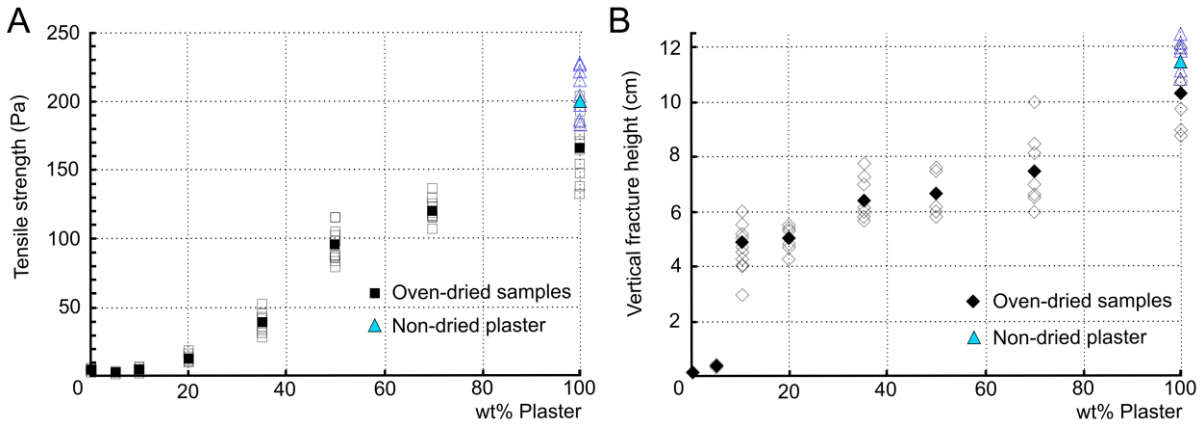


**Figure 9 – A.** Tensile strengths ($T_0$) of sand and plaster and their mixtures as measured in tensile tests on oven-dried samples compacted by manual tapping. Unfilled symbols indicate individual measurements and therefore the uncertainty on the averages represented by the filled icons; **B.** Heights H of the vertical upper portions of normal (graben) faults formed in sand and plaster and their mixtures measured in extensional tests on oven-dried samples compacted by manual tapping. Unfilled icons show individual measurements and therefor indicate the uncertainty on the averages represented by the filled icons. Triangles in A. and B. represent individual measurements on air-dried plaster in equilibrium with laboratory ambient air humidity (20-30%).

**Table 3** – Physical properties of mixtures of oven-dried and compacted mixtures of quartz sand and plaster: tensile strength, vertical height of opening-mode fractures measured in extension tests, and Griffith cohesion $C_G$ derived from the former two parameters (bent lower part of failure envelope); * marks non-dried plaster in equilibrium with ambient air humidity.

| Sand:Plaster ratio (wt%) | $T_0$ (Pa) | H (cm) |
|---|---|---|
| 100:0 | 5±1 | 0.1±0.5 |
| 95:5 | 2±1 | 0.4±0.8 |
| 90:10 | 5±1 | 4.9±0.4 |
| 80:20 | 13±3 | 5.0±0.4 |
| 65:35 | 39±7 | 6.4±0.7 |
| 50:50 | 96±13 | 6.6±0.7 |
| 30:70 | 121±8 | 7.5±1.3 |
| 0:100 | 166±24 | 10.3±1.1 |
| 0:100* | 200±18 | 11.5±0.6 |

## 5. Failure criterion analysis: Cohesion and friction coefficients

### 5.1 Theoretical background

While Coulomb proposed a linear failure criterion, the stresses at failure (peak strength) for most natural rocks of the upper part of the crust correspond to a non-linear failure envelope in shear stress - normal stress space (Byerlee, 1978; Jaeger et al., 2007 and references therein), especially at the lower normal loads governing laboratory experiments (Mourgues and Cobbold, 2003). We determined the optimal fit of failure envelope to sand-plaster mixtures, by applying a linear Coulomb failure criterion and a non-linear Griffith failure criterion to the combined results from tensile tests and direct shear tests.

The Coulomb failure criterion describes a linear relationship between the shear stress $\tau$ on the failure plane and the effective normal stress $\sigma_n$ acting on that plane:

(7) $\tau = \mu_C \sigma_n + C_C$,

where $\mu_C$ is the Coulomb coefficient of internal friction or the slope of the line and $C_C$ the Coulomb cohesion ('apparent' cohesion in Abdelmalak et al., 2016) derived from the intercept of the failure envelope with the y($\tau$)-axis in a Mohr space diagram (Figure 1C). Such a linear relationship is commonly used to describe shear failure at relatively high normal stresses (i.e. high confining pressures, and thus greater depth) acting on rocks in the upper crust (Byerlee, 1978).

At low and negative (tensile) normal stresses (i.e. low confining pressure, and thus depth or with high fluid pressures), a non-linear failure envelope has been invoked to account for

tensile and hybrid tensile/shear failure. One commonly used non-linear envelope is the parabolic Griffith criterion (Jaeger et al., 2007; Labuz et al., 2018):

(8) $\tau^2 = aT_0 (\sigma_n + T_0)$,

Where a is a material-dependent constant and $T_0$ is the tensile strength determined by the $x(\sigma_n)$-axis intercept of the failure envelope in a shear - normal stress diagram (Figure 1C). Where the criterion intercepts the $y(\tau)$-axis of the failure envelope, it defines the Griffith cohesion $C_G$ of the material:

(9) $C_G = T_0 \sqrt{\frac{a}{T_0} + 1}$.

For some uncompacted cohesive powders used in laboratory experiments, $a \approx 2$ has been found (Mourgues and Cobbold, 2003) but compacted silica powder shows $a \approx 3$ (Galland et al., 2006), while for lactose and corn starch powders $a \approx 4$ (Schweiger and Zimmermann, 1998). Abdelmalak et al. (2016) provide a more general treatment of the origin of these values.

Fitting of Coulomb and Griffith failure criteria to the shear strength and/or tensile strength data was applied by using an adaptation of the 'RST evaluation' Python script (Rudolf and Warsitzka, 2019). The Coulomb cohesion $C_C$ and the Coulomb friction coefficient $\mu_c$ were obtained by a 100-fold linear least-squares regression of the data plus noise to find the optimal fit of the linear Coulomb failure criterion in equation (7). The Griffith cohesion $C_G$ was obtained by a 100-fold non-linear least-squares regression of the data plus noise to find the optimal fit of parameters a and $T_0$ in equation (8).

In general, we used both direct shear test data and tensile test data to constrain optimal Coulomb and Griffith criteria for each of the oven-dried and compacted end-member materials and their mixtures, and for non-dried poured+compacted plaster (Figure 8). We then choose the best-fitting of these criteria to derive either a Coulomb cohesion ($C_C$) or a Griffith cohesion ($C_G$) value for each material. Since the slope of the Griffith criterion is non-unique, we used by default the optimal Coulomb criterion to derive a friction coefficient ($\mu_C$) for each material.

We used only the peak strength data from the ring shear test results (poured, sieved, oven-dried and poured+compacted) to constrain an optimal Coulomb criterion as that is a standard approach in such tests (Klinkmüller et al., 2015; Montanari et al., 2017; Panien et al., 2006; Schulze, 1994). For comparison to the ring shear test results, we used only the shear strength data from the direct shear tests to constrain a Coulomb criterion for each material. This also enabled us to evaluate the added value of tensile test results in the failure criterion fitting.

Finally, we combined average tensile strength from tensile tests with the vertical height of opening-mode fractures measured in extension tests to estimate the Griffith cohesion $C_G$ of the materials. This approach follows the method proposed by Abdelmalak et al. (2016) and uses the approximation:

(10) $C_G = T_0 \sqrt{\frac{H \rho g}{T_0} + 1}$.

## 5.2 Failure criterion fitting results

A selection of the derived Coulomb ($C_C$) and Griffith ($C_G$) cohesions (Table 4) and friction coefficients ($\mu_C$) (Table 5) is displayed in Figure 10. For sand and sand-plaster mixtures with plaster contents < 35 wt%, $C_C$ values from combinations of tensile strength data and direct shear data (Figure 10A, green circles) yield the optimal fits (i.e. standard deviations are smaller with respect to the cohesion values, see Table 4). $C_G$ values obtained from tensile and extension test data (Figure 10A, red squares), which are constrained only from data in the tensile field, lie within the double standard deviations of $C_C$ values, and increase from < 10 Pa to ~105 Pa (Table 4).

**Table 4** – Cohesions of oven-dried and poured+compacted sand, plaster and sand-plaster mixtures obtained from optimal fitting of linear Coulomb ($C_C$, $\mu_C$) and non-linear Griffith ($C_G$) failure criteria to various combinations of tensile strength, direct shear and ring shear test results, and tensile strengths $T_0$ and heights H of opening-mode fractures; * marks air-dried plaster.

| Sand: Plaster ratio (wt%) | $C_C$ direct shear + $T_0$ (Pa) | $C_C$ direct shear (Pa) | $C_C$ ring shear compact (Pa) | $C_C$ ring shear poured (Pa) | $C_C$ ring shear sieved (Pa) | $C_G$ direct shear + $T_0$ (Pa) | $C_G$ ($T_0$ + H) (Pa) |
|---|---|---|---|---|---|---|---|
| 100:0 | **4±21** | 13±69 | 214±27 | 252±163 | 195±44 | 33±3 | 9.8±0.1 |
| 95:5 | **12±24** | 61±63 | 166±24 | - | | 36±3 | 12.8±0.1 |
| 90:10 | **16±29** | 77±80 | 168±26 | 359±204 | 15±55 | 58±4 | 66.2±0.1 |
| 80:20 | **18±28** | 67±76 | 269±27 | 297±137 | 174±160 | 99±3 | 104.8±0.1 |
| 65:35 | 59±38 | 240±84 | 400±55 | - | - | **154±7** | 195.2±0.1 |
| 50:50 | 105±30 | 275±51 | 452±21 | 474±110 | 391±204 | **222±9** | 297.9±0.1 |
| 30:70 | 106±27 | 256±25 | 240±21 | - | - | **233±7** | 340.5±0.1 |
| 0:100 | 127±26 | 248±49 | 233±21 | - | - | **250±21** | 425.2±0.1 |
| 0:100* | 157±22 | 192±68 | - | 672±105 | 615±85 | **282±24** | 494.9±0.1 |

For sand-plaster mixtures with plaster contents ≥ 35 wt%, $C_C$ values systematically overestimate the lower part of the failure envelope, whereas $C_G$ provides optimal fit (Figure 10, orange circles). For direct shear test data alone in comparison, $C_C$ provides larger standard

deviations and thus poorer fits (see Table 4). $C_G$ values obtained from tensile strength and direct shear data (Figure 10, orange circles) first continue increasing, albeit at a lower rate > 50 wt% plaster, until the maximum of ~280 Pa for pure plaster. $C_G$ values obtained from tensile and extension tests increase roughly linearly ($R^2 = 0.965$) with increasing wt% plaster content until a maximum of ~500 Pa for non-dried compacted plaster (Table 4, Figure 10A).

Overall, the $C_C$ values derived from ring shear data (Figure 10, green diamonds) are strongly dependent on the higher normal stress data (5000 Pa) and their standard deviations are systematically higher compared to those obtained from all other methods (Table 4). Their $C_C$ values are highest of all obtained values for mixtures with plaster content ≤ 50 wt%, but abruptly decrease to values similar to $C_G$ values derives from failure envelopes that combine tensile and direct shear test data. $C_C$ values derived from direct shear data alone do not show obvious trends, but they systematically have higher standard deviations compared to those obtained from failure envelopes that combine tensile and direct shear test data and are therefore not displayed on Figure 10A. Air-dried plaster yielded a $C_G$ value that is ~50 Pa higher compared to oven-dried plaster, and displays relatively higher standard deviations (Table 4, Figure 10A, blue-and-red circle).

Friction coefficient values can only be derived using a linear Coulomb criterion (Figure 10B, Table 5). $\mu_C$ values derived from tensile strengths and direct shear data (Figure 10B, green circles) increase with increasing plaster content up to ≤ 20 wt%. For mixtures with a plaster content ≥ 35 wt%, $\mu_C$ values decrease again to about half of the value for plaster obtained from ring shear data.

$\mu_C$ values obtained from ring shear data (Figure 10B, green diamonds) have much lower standard deviations compared to those from combined tensile strengths and direct shear data (Figure 10B, green circles), but produce no discernable trend. Values varie between 0.71 and 0.81, with an outlying minimum of 0.63 for non-dried plaster (Table 5).

$\mu_C$ values of non-dried plaster obtained either from direct shear data alone, or in combination with tensile test data, agree very well (Table 5, Figure 10B, blue-and-red circle). These values are slightly higher than those obtained for oven-dried plaster as constrained from tensile strength and direct shear test data (Figure 10B, green circles), and they are lower than those for oven-dried plaster as constrained from ring shear test data (Figure 10B, diamonds).

**Table 5** – Friction coefficients of oven-dried and compacted mixtures of quartz sand and plaster obtained from optimal fitting of linear Coulomb (μc) failure criteria to failure envelopes of various combinations of tensile strength, direct shear and ring shear test results; * marks non-dried plaster in equilibrium with ambient air humidity.

| Sand:Plaster ratio (wt%) | $\mu_C$ direct shear + $T_0$ | $\mu_C$ direct shear | $\mu_C$ RST compact | $\mu_C$ RST poured | $\mu_C$ RST sieved |
|---|---|---|---|---|---|
| 100:0 | 0.54±0.08 | 0.48±0.08 | 0.70±0.01 | 0.64±0.02 | 0.67±0.01 |
| 95:5 | 0.85±0.10 | 0.61±0.08 | 0.80±0.01 | - | - |
| 90:10 | 0.88±0.12 | 0.85±0.13 | 0.77±0.01 | 0.78±0.02 | 0.82±0.01 |
| 80:20 | 0.96±0.08 | 0.85±0.09 | 0.70±0.01 | 0.80±0.01 | 0.76±0.01 |
| 65:35 | 0.72±0.12 | 0.55±0.11 | 0.81±0.02 | - | - |
| 50:50 | 0.65±0.11 | 0.48±0.08 | 0.72±0.01 | 0.88±0.01 | 0.85±0.02 |
| 30:70 | 0.59±0.08 | 0.41±0.03 | 0.77±0.01 | - | - |
| 0:100 | 0.56±0.08 | 0.43±0.08 | 0.76±0.01 | - | - |
| 0:100* | 0.66±0.10 | 0.63±0.06 | 0.63±0.06 | 0.80±0.01 | 0.83±0.01 |

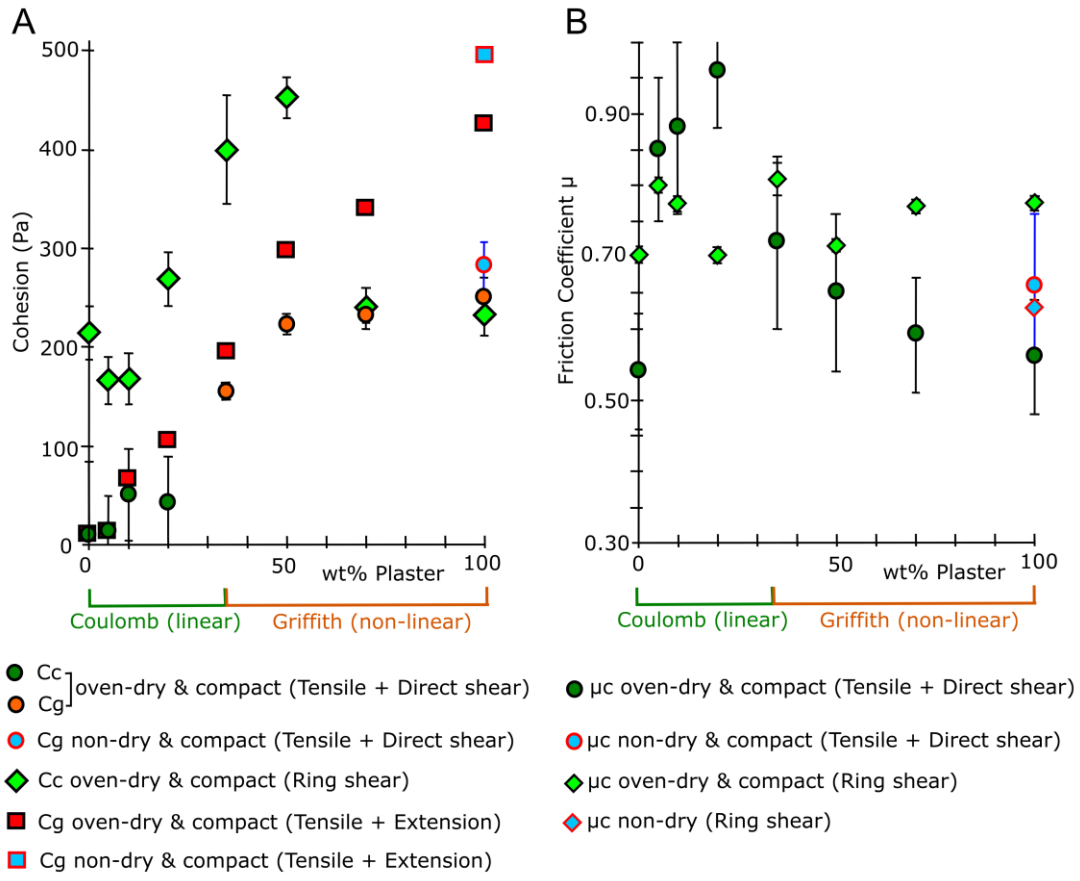


**Figure 10** – Regression results based on failure envelope reconstructions in shear-normal stress space using a linear Coulomb failure criterion versus a non-linear Griffith one. **A.** Cohesion of compacted sand, plaster and sand-plaster mixtures. Best-fit $C_C$ (< 35 wt% plaster) or $C_G$ (> 20 wt% plaster) values are displayed for the combination of tensile and direct shear tests. Ring shear results are peak shear strengths. See Table 4. **B.** Friction coefficient values $\mu_C$ of compacted sand, plaster and sand-plaster mixtures for the combination of tensile and direct shear test data or ring shear test data. See Table 5.

## 6. Discussion

### 6.1 Impact of material handling and humidity on material properties

It is well established that the mechanical properties of quartz sand differ significantly when emplaced into a sand-box by sieving or pouring. Sieving produces a sand pack with higher density, higher internal friction coefficient and a more brittle stress-strain behaviour – i.e. a sharper stress peak and a larger post-peak stress drop (Lohrmann et al., 2003; Panien et al., 2006). For pure quartz sand, our tests reproduce such observations (Figures 4 and 6, Table 2). This difference in behaviour between sieved and poured sand can be attributed to slower sedimentation rates during sieving, which allows grans to saltate, creep and resettle in to a tighter grain packing. Density of pure sand can be further elevated by compaction – either through pressing (ring shear tests) or vibration (tapping). Our data indicate that compaction does not give a discernable effect on cohesion (Table 4), but that it slightly increases the friction coefficient of pure sand (Table 5).

For pure plaster, our tests document the opposite behaviour: sieved plaster is less dense, poured plaster more dense (Figure 4B, Table 2). For a sand-plaster mixture with a plaster content of 50 wt%, there is no significant difference in the density when sieved or poured. We propose that friction with air during sieving might result in increased electro-static forces that increase porosity between settled plaster grains (van Gent et al., 2010). On the other hand, pouring plaster may reduce electrostatic forces and, if done at once, may make plaster-rich packs more susceptible to compaction during emplacement. In terms of mechanical properties, our data show that sieved plaster compacts more at low normal loads compared to poured plaster (Figure 6). Sieving or pouring of pure, air-dried plaster did produce a discernable difference in cohesion (Table 4), and sieving may slightly increase the friction coefficient (Table 5). Compaction and drying in combination have a strong effect on the mechanical behaviour of pure plaster, however. In addition to higher bulk density and smoother stress-displacement curves, a more brittle behaviour is seen at low normal loads compared to poured or sieved plaster (Figures 6 and 7), and cohesions and friction coefficients are lower regardless of shear testing approach and failure envelope reconstruction (Tables 4 and 5). This may be because compaction flattens more tabular gypsum crystals toward alignment with the shear plane, thus making grain-grain sliding easier, and/or because reduced moisture content reduces the electrostatic attractions between plaster grains.

For sand-plaster mixtures, and in addition to density differences, sieving results in layered, non-homogeneous grain size distribution throughout packs (Figure 4A). Thus, sieving devices that are designed to ensure an ideally dense packing of sand (e.g. Maillot 2013) would create

heterogeneous layering due to density differences between quartz sand and gypsum particles. Similarly, Krantz (1991) showed that such density differences induced by the emplacement technique affect the shear strength of mixtures of quartz sand and cement more than the grain density differences between the sand and cement. Pouring is also not ideal as it creates variations in grain packing density throughout sand-plaster mixtures. We surmise that these effects of pouring or sieving could be seen in our data to some extent. Poured samples, as well as sieved samples with high plaster content, generally show noisier stress-displacement curves (Figure 6), although no clear trends or differences were seen in cohesion and friction values (Tables 4 and 5). Compaction and oven-drying had a strong effect on pure plaster. Smoother stress-displacement curves, a more brittle behaviour (stress drop) at low normal loads, and lower friction coefficients are consistently seen compared to non-dried and non-compacted equivalents (Table 4).

The problem of ambient humidity in granular analogues has received little attention, although in quartz sand, moisture is known to increases the bulk strength (van Mechelen, 2004). Sand-plaster mixtures in past studies have been used in equilibrium with ambient air humidity in laboratories, which can vary strongly from day to day influenced by the weather. Our data demonstrate that a sand-plaster mixture's humidity increases with increasing plaster content (Figure 5). The moisture uptake by gypsum powder from ambient humidity was previously measured to be ~2-2.5 wt% over 2.5 days under a constant air humidity of 75.2% (Lide, 1995). Undried plaster used here contains on average 1 wt% of water (Figure 5). Our data further show that comparative test results of direct shear, tensile strength, and extension fracturing of pure air-dried plaster are statistically distinct from those of oven-dried plaster (Figures 8, 9 and 10). The strength of non-dried plaster is thus significantly affected by humidity. Importantly, the measurement uncertainties of the mechanical properties of non-dried plaster are higher as well. Our results establish that oven-drying sand-plaster mixtures to remove excess humidity prior to emplacement in a modelling apparatus should be pursued to increase reproducibility of the physical properties of the mixtures.

Except for Poppe et al. (2019), published experimental laboratory studies do not mention oven-drying sand-plaster mixtures prior to experimentation. Poppe et al. (2015) invoked variations in humidity of the sand-plaster mixtures from day to day to explain the occurrence of overburden stability in some experiments and overburden collapse in other experiments. In other experimental studies of geological deformation, the dip of fault planes formed in non-dried, poured sand-plaster piles has been systematically measured (Holohan et al., 2013; Rincón et al., 2018; Roche et al., 2001). That dip, however, depends on the angle of internal

friction, which our results demonstrate in turn depends on material humidity and compaction. Furthermore, asymmetric development of model deformation in laboratory models of volcanic processes where cones have been traditionally poured has been attributed to set-up geometry asymmetry (e.g. Byrne et al., 2013; Delcamp et al., 2008; Kervyn et al., 2009; Merle and Borgia, 1996; Rincón et al., 2018; Van Wyk De Vries and Merle, 1998). Our results show that humidity and bulk density – i.e. porosity – variations may cause spatial and temporal heterogeneities in the mechanical properties of sand-plaster mixtures that are unaccounted for.

Based on our results, we recommend oven-drying and compacting sand-plaster mixtures prior to their deformation in scaled laboratory models. Sand-plaster mixture ratios should be calculated by weight% (this study; Poppe et al., 2019) rather than by volume% (e.g. Delcamp et al., 2008; Poppe et al., 2015; Rincón et al., 2018; Roche et al., 2000; Zorn et al., 2020). Immediately after drying, mixtures should be cooled in a sealed container to prevent reabsorption of air moisture. During model set-up, a known mass of the mixture should be instantaneously poured into the sand-box and mechanically compacted down to a pre-determined bulk volume and thus a well constrained bulk density. That compaction can be achieved by manual tapping as in our direct shear, tensile and extension tests, by pre-loading and pressing the samples as in our ring shear tests, or by mechanical vibration (Galland et al., 2009; Poppe et al., 2019). Such a more consistent approach to material handling should help to better constrain bulk densities and porosities, to ensure homogeneous grain size and mineralogy distribution, to provide better control on mechanical properties, and promote greater confidence in the reproducibility of experimental outcomes involving sand-plaster mixtures.

### 6.2 The silo effect in direct shear tests : empirical versus theoretical correction

In a silo, side-wall friction counteracts gravity forces; this ‘silo effect’ or ‘Jansen effect’ reduces the actual normal load acting on the shear plane in a direct shear test (Jansen, 1895). Most often, the linear Coulomb failure criterion is assumed to adequately fit failure envelopes of quartz sand that are reconstructed from direct shear tests, and quantify the sand’s cohesion and friction coefficient (e.g. Galland et al., 2006; Krantz, 1991; Lohrmann et al., 2003; Montanari et al., 2017; Schellart, 2000). When corrected theoretically for the silo effect, the failure envelopes gain a steeper slope and their intercept with the vertical axis decreases in absolute value (Mourgues and Cobbold, 2003). Mourgues and Cobbold (2003) set a theoretical threshold of sample height to cylinder diameter ratio of 0.5 to avoid the silo effect.

That ratio is nevertheless as high as 1 in other studies (Abdelmalak et al., 2016; Schellart, 2000). If unaccounted for, the silo effect results in underestimated internal friction coefficients and overestimated cohesions.

We have found empirically that side-wall friction progressively reduces the normal load at the failure plane in direct shear tests, even at low normal loads below that theoretical threshold value of 0.5 (see Supplementary Materials). Furthermore, we found that the silo effect increases with increasing plaster content, up to about 50 wt% plaster and then it decreases slightly, although it remain higher for pure plaster than for pure sand. Our empirical correction method yielded reduced effective normal loads, and thus produced failure envelopes with steeper slopes and with lower vertical axis intercepts in shear-normal stress space. As a result, the cohesion values of granular materials in past studies that ignore the silo effect are most likely overestimations (e.g. Abdelmalak et al., 2016; Lohrmann et al., 2003; Schellart, 2000). Similarly, friction coefficients estimated previously from direct shear tests without silo effect correction are likely underestimates. This empirical correction can be used when establishing new granular analogue materials, or retrospectively to correct published direct shear test results.

### 6.3 Effects of plaster content on mechanical properties

Our data show that for several measured physical or mechanical properties, such as bulk density, porosity, tensile strength, derived cohesions and friction coefficients, as well as the brittle or ductile behaviour of the material, are sensitive to the plaster content in a mixture regardless of handling procedure. In addition, trends in these properties differ for sand-rich mixtures (i.e. $\leq$ 20 wt% plaster content), compared to plaster-rich mixtures (i.e. $\geq$ 35 wt% plaster contents).

With increasing plaster content, there is an overall decrease in bulk density of a sand-plaster mixture and a corresponding increase in porosity (Figure 4B & C). Moreover, there is a notable increase in the rate of change of density or porosity with increased plaster content at 20 wt% plaster content and higher. The bulk density of plaster is approximately half that of quartz sand, for the same handling and humidity (Figure 4B). Conversely, the inferred porosity of quartz sand is 35-55 vol% and that of plaster is 65-78 vol% (Figure 4C). Previously, van Gent et al. (2010) found a similar porosity of ~75 vol% for gypsum powder.

SEM images and grain size distribution measurements showed that smaller gypsum crystals (mean diameter of 2-10 μm) aggregate into clusters (Figure 2), which are too large to fill the pore space in between the larger sand grains (mean diameter of 180-250 μm). Therefore,

although gypsum crystals have slightly greater density than quartz crystals (2730 $kg.m^{-3}$ vs. 2655 $kg.m^{-3}$), the bulk density of a sand-plaster mixture decreases as the plaster content increases because of the high micro-scale porosity of the gypsum aggregates (Figure 4B).

An increase in plaster content also generally leads to a more ductile behaviour of a sand-plaster mixture (Figures 6 & 7). The stress drop seen for sand-rich mixtures diminishes and ultimately disappears, especially at high normal stresses (<1000 Pa). An exception is when the mixture is oven-dried and pre-compacted; then a small stress drop persists in plaster-rich materials at low normal stresses (<1000 Pa). Irrespective of handling technique, the stress drop diminishes from about 20-35 wt% plaster content and upward. This general shift to a more ductile behaviour in stress-displacement curves as plaster content increases corresponds to a change in dilation behaviour. Sand-rich mixtures (<35 wt% plaster) compact prior to sample failure then de-compact, as previously observed for pure sand (Panien et al., 2006; Ritter et al., 2016). Plaster-rich samples (>35 wt% plaster) undergo compaction throughout shearing. Numerical simulations of deformation of granular materials produce a similar transition to more ductile and compaction-dominated behaviour with increased porosity (cfr. Figure 4 in Schöpfer et al., 2009). Therefore, we tentatively attribute the change to a more ductile behaviour with increased plaster content to increased bulk porosity. This change may occur with more distributed strain localisation in the more porous plaster-rich mixtures, especially at high normal stresses, as the progressive collapse of pore-spaces in the gypsum crystal aggregates inhibits the formation of well-defined shear zones.

Sand-plaster mixtures therefore have the capacity, like real rocks, to display a brittle-ductile transition with depth. Considering the normal stress as equivalent to confining pressure of an overburden and assuming the compacted bulk densities in Table 2, that transitional depth would amount to 30 cm height (i.e. at ~5000 Pa) in mixtures with 20 wt% plaster. This depth would be shallower with increased plaster content, and it would lie at ~16 cm (~2000 Pa) with 50 wt% plaster and at 11 cm (~1000 Pa) in pure plaster. This brittle to ductile transition primarily represents a change in strain-weakening or strain-strengthening behaviour, and does not necessarily imply a major change in strain localisation (i.e. shear zone vs. distributed flow) with depth within a material.

Associations between increased plaster content and a sand-plaster mixture's strength, in terms of cohesion and friction coefficient, are complex and in part dependent on measurement technique. In general, cohesion increases with increasing plaster content, up to about 50 wt % plaster (Figure 10A, Table 4). Coulomb cohesions thereafter decrease or stabilize, whereas Griffith cohesions continue to increase with increased plaster content. Friction coefficient

971 either shows no clear trend with increasing plaster content (ring shear test data) or shows an
972 initial slight increase at 0-20 wt% plaster followed by overall decrease at 20-100 wt% plaster
973 (Figure 10B, Table 5). Uniaxial compressive strength of quartz crystals at room temperature
974 and pressure is around 190-300 MPa (and references therein Scholz, 1972), whereas ultimate
975 shear strength of gypsum crystals is around 0.6 – 18 MPa (Williams, 1988). Such crystal
976 strengths far exceed the differential stresses applied in our material tests. The friction
977 coefficient of granular materials in a regime of no grain fracture is known to increase with
978 increased grain surface roughness (angularity) and particle size distribution (Mair et al.,
979 2002), however, and it is known to decrease with increased porosity (Schöpfer et al., 2009).
980 Moreover, stick-slip behaviour in deformed granular materials is associated with smoother
981 grain surfaces (Mair et al., 2002; Rosenau et al., 2009). Therefore, we interpret that cohesions
982 and friction coefficients at plaster contents of up to 20-50 wt % initially increase because of
983 increased particle size distribution on mixing relatively coarse quartz sand with relatively fine
984 gypsum powder (Figure 2). Increased inter-crystal attraction forces in gypsum may also play a
985 role in that initial strength increase (see below). Cohesion and friction coefficient
986 subsequently decrease or stabilize at plaster contents of up to 50-100 wt % because of
987 increased porosity (Figure 4) and possibly also the capability of gypsum grains to align and to
988 slip past each other along their relatively smooth crystal faces. The latter factor can also
989 account for the short-frequency noise and stick-slip events observed in plaster-rich mixtures
990 (Figure 6 & 7).
991 Increasing plaster content of sand-plaster mixtures is clearly associated with increased tensile
992 strength. This has been known qualitatively from the occurrence of opening mode fractures in
993 such mixtures compared to the absence of such fractures in pure quartz sand, and has formed
994 a main reason for use of plaster veneers or sand-plaster mixtures previously (e.g. Byrne et al.,
995 2013; Holohan et al., 2008; Poppe et al., 2015; Roche et al., 2001; Shea and van Wyk de
996 Vries, 2008; van Gent et al., 2010). Here, we quantify the tensile strength increase, and we
997 show again that its rate increases sharply at ≥ 20 wt% plaster content (Figure 9A). The high
998 tensile strength of plaster relative to quartz sand, and the corresponding increase in tensile
999 strength with increased plaster content in mixtures, are potentially related to the increased
1000 effectiveness of electrostatic attraction forces that bond gypsum crystals. Tensile strength has
1001 been shown to decrease slightly with porosity in numerical simulations of the deformation of
1002 granular material, but to increase greatly with increased proportion of bonded contacts
1003 between particles (Schöpfer et al., 2009). Atomic Force Microscopy experiments show that
1004 gypsum crystal faces are attracted to each other by van der Waal's forces and electrostatic

forces, which are supplemented by capillary forces at high relative humidity (Finot et al., 2001). In general, therefore, an increase in such attraction forces with increased plaster content in sand-plaster mixtures can account for the increased tensile strength of such mixtures. The increase in inter-crystal force attraction with increased humidity also explains the still greater tensile strength of pure undried plaster. Overall, these data confirm that using plaster as a filler in sand is a valid strategy to increase and control such a mixture's tensile strength.

### 6.4 Empirically reconstructed failure envelopes and theoretical failure criteria

Ring shear tests and direct shear tests on oven-dried and pre-compacted samples give slightly different failure envelopes in the compressive stress field and consequently give different values of cohesion and friction coefficient (Tables 4 & 5, Figure 10). While ring shear tests reportedly yield accurate estimates of friction coefficients of sands with low standard deviations, the method has yielded unrealistically high cohesions with large standard errors from linear Coulomb extrapolations (Klinkmüller et al., 2015; Montanari et al., 2017; Panien et al., 2006; Ritter et al., 2016). Furthermore, ring shear tests are difficult to operate at small normal loads (<500 Pa), whereas direct shear tests are better suited to constrain this lower part. Ritter et al. (2016) inferred that in ring shear tests the through-going shear zone likely develops via the linkage of several shear zones, each initiated at one of the intruding lid blades. In contrast, a through-going shear zone likely develops more readily as a single shear failure plane in direct shear tests. This contrast in test methodology may at least partially explain the mismatch between failure envelopes derived from ring shear test results and direct shear test results (Figure 8), and consequently the values of cohesions and friction coefficients derived from the linear Coulomb criterion (Figure 10).

Cohesion values obtained for oven-dried and pre-compacted sand-plaster mixtures by extrapolation of shear strength only ($C_C$) shows different trends to those obtained by extrapolation of tensile strength and extensional test data only ($C_G$) (Table 4). Cohesions from direct shear test or ring shear tests, despite differences in absolute values, show a similar initial increase at low plaster contents followed by a decrease or levelling off at high plaster contents (Figure 10). In comparison, cohesions obtained from combining tensile strength data with extension tests yield a more monotonic linear increase of cohesion from near-zero for sand to >400 Pa for plaster. The latter method is based on a non-linear Griffith criterion that ignores data in the compressive field (Abdelmalak et al., 2016), however, and the resultant

monotonic increase in cohesion that it yields is highly dependent on the measured value of tensile strength (Equation 10), which itself increases linearly with plaster content (Figure 9). In general, we therefore regard the cohesion and friction values constrained by interpolation between data in both tensile and compressive fields to be more reliable than those constrained by extrapolation from data in one field only. We find that linear Coulomb failure criteria more optimally fit the combined tensile strength and direct shear data of sand-rich mixtures (<35 wt% plaster), whereas non-linear Griffith failure criteria better fit the combined tensile and shear data of sand-plaster mixtures with ≥35 wt% plaster content. The addition of tensile strength data in criterion fitting considerably helps to constrain the lower – negative – part of the failure criteria (Table 4, Table 5). The resulting 'preferred' cohesion values (Figure 10A) increase from near-zero for pure quartz sand to 200-250 Pa for sand-plaster mixtures with ≥ 50 wt% plaster. Similarly the 'preferred' friction coefficient values derived from Coulomb criteria fitted to data in both tensile and compressive fields (Figure 10B) increase from ~ 0.54 for pure quartz sand to ~ 0.96 for mixtures with 20 wt% plaster and then decrease to ~0.56 for pure plaster. The more optimal fit of a non-linear Griffith failure criterion to sand-plaster mixtures with a plaster content ≥35 wt%, shows that, in detail, the internal friction coefficient of such mixtures is not constant throughout a sandbox model, but rather varies with depth – as is the case for rock masses in nature. The fit of other non-linear failure criteria, such as that of Hoek-Brown (Jaeger et al., 2007; Labuz et al., 2018) for such mixtures could be explored in the future.

### 6.5 Implications for scaling analogue models of crustal deformation

The combination of mechanical laboratory tests has shown that by systematically controlling the weight ratio of quartz sand to plaster, analogue granular materials of varying strengths but also brittle to complex brittle-ductile shear stress behaviour can be obtained. Compared to pure sand, these properties allow analogue modelers to simulate a greater range of tensile to shear fracturing, brittle to ductile behaviour, similar to how natural rocks are known to behave in the shallow crust (e.g. Byerlee, 1978, 1968; Jaeger et al., 2007). Our characterisation now quantifies values of cohesions and friction coefficients for sand-plaster mixtures (Tables 4 and 5) and shows that they are suitable to simulate natural rock strengths in scaled laboratory models (Table 1). The comparison of failure criteria fits, however, also exposes the uncertainties related to applying theoretical models to describe the complex, non-linear rheology of granular analogue materials. Tensile strengths, in addition, might provide a complementary or more direct means to scale laboratory experiments where opening-mode

failure is important. This is the case for example in simulations of magma-filled fracture opening that forms sheet intrusions (Galland et al., 2018; Poppe et al., 2019; Rivalta et al., 2015), or in some tectonic extension experiments (e.g. Reber et al., 2020; Schreurs et al., 2006). The newly quantified values of tensile strength, cohesion and friction coefficient of sand-plaster mixtures now allow to systematically explore the effect of analogue granular material strength as an experimental parameter.

## 7. Summary and conclusions

Our study confirms that mixtures of quartz sand and gypsum powder – i.e. plaster – possess brittle to brittle-ductile behaviour that is analogue to that of crustal rocks. Using density measurements and ring shear tests, we have constrained the effect of the emplacement technique – i.e. sieving, pouring and pouring+compaction – and humidity on the physical properties of a range of sand-plaster mixtures. Ring shear tests allowed a detailed characterisation of the stress-displacement behaviour. We used complementary direct shear tests, tensile tests and extensional tests to constrain the shear and tensile strengths of density-controlled, oven-dried samples of sand, plaster and sand-plaster mixtures.

When emplacing an experimental volume of sand-plaster granular material, we found that:

- Sieved sand is denser and less porous compared to poured sand; sieved plaster is conversely less dense and more porous compared to poured plaster; the effects for sand-plaster mixtures lie in between their two end-members.
- Sieving sand-plaster mixtures introduces compositional and bulk density heterogeneity in the form of layering. Pouring sand-plaster mixtures leads to under-compaction and very high porosity and possibly to lateral variations in these. Pouring followed by mechanical compaction produces more controlled and laterally consistent density while minimizing mineralogical heterogeneity.
- Plaster contains at least 1 wt% moisture.
- Humidity increases the strength of plaster and increases the uncertainty in the measured mechanical properties.

To obtain reproducible composition and mechanical properties, we recommend that sand-plaster mixtures should be oven-dried for at least 24 hours to remove ambient humidity and be poured and compacted mechanically to a controlled bulk density.

The stress-displacement behaviour of sand-rich sand-plaster mixtures ($\leq$ 20 wt% plaster) is dominantly brittle, while plaster-rich sand-plaster mixtures ($\geq$ 35 wt% plaster) exhibit more complex, brittle-ductile behaviour. The documented brittle-ductile transition is thus

constrained by the plaster content and the applied normal stress. We infer that this transition is ultimately controlled by a porosity increase with increasing plaster content.

For oven-dried, poured and compacted sand-plaster mixtures, a linear Coulomb failure criterion fits most optimally to failure envelopes for ≤ 20 wt% plaster as constrained by both tensile strength and direct shear test data. A non-linear Griffith failure criterion most optimally fits the failure envelopes for sand-plaster mixtures with ≥ 35 wt% plaster. Our comparison of empirical mechanical testing methods suggests that the best-fit cohesions most likely range from ~0 Pa for quartz sand to ~250 Pa for pure plaster, while friction coefficients estimated from a linear Coulomb criterium range from 0.50 to 0.94, respectively. The more optimal fit to a non-linear failure criterion suggests that in detail friction coefficients likely vary with depth within a sand-plaster mixture with ≥ 35 wt% plaster. The relationship of cohesion and friction coefficient to plaster content is non-linear, and likely reflects a complex interplay of factors controlling material strength, such as porosity, grain shape, grain smoothness, particle size distribution and attraction forces between gypsum crystals.

We found that absolute tensile strength of a sand-plaster mixture increases near-linearly with increased plaster content from near-zero for pure quartz sand to 166±24 Pa for pure plaster. This value also increased with increased humidity. The tensile strength of sand-plaster mixtures likely derives from attractive forces (van der Waal's, electrostatic and capillary) acting between gypsum crystals.

Overall, this detailed characterisation effort quantifies the range of tensile, shear-failure, brittle to ductile behaviour of natural rocks in the Earth's upper crust that can be simulated by analogue sand-plaster mixtures in scaled laboratory experiments. Using the best-practice recommendations for mechanical testing of granular sand-filler materials, material handling and emplacement, and the characterised mechanical properties, will provide a more robust basis for using sand-plaster mixtures in laboratory-scale simulation of natural rock-mass deformation.

## Author contributions

SP led all phases of this study, including writing the manuscript as part of his PhD research defended in 2019 at VUB, Belgium. SP's thesis was co-supervies by MK and EPH. EPH, OG, MR, MR, AD and MK contributed to the experimental planning, interpretation of the results and revision of the manuscript. EPH and MRo provided advice and access to the RST machine at GFZ Potsdam, Germany. MRu collected RST data on compacted sand-plaster mixtures at GFZ Potsdam and produced figures 6 and 7, SP collected all other data.

## Declaration of interest statement

The authors declare that they have no known competing financial interests or personal relationships that could have appeared to influence the work reported in this paper.

## Data availability

The original data collected for this study is available as part of the GFZ open-access data publication Poppe et al. (2021), https://doi.org/10.5880/fidgeo.2021.005, completed with mechanical test data for garnet sand and kaolin clay powder mixed with quartz sand as used in Grosse et al. (2020).

## Acknowledgments

SP was supported during 2014-2019 by an Aspirant PhD fellowship from the Flemish Fund for Scientific Research FWO-Flanders, Belgium, and a Vocatio grant, and since October 2020 by a frs-FNRS postdoctoral fellowship at ULB, Brussels. MRu and MRo have been supported by the Deutsche Forschungsgemeinschaft (DFG) through grant CRC 1114 "Scaling Cascades in Complex Systems", Project Number 235221301, Project B01. R. Mourgues granted access to the tensile test apparatus of the Geology Department of the University of Maine, France, and kindly donated the Hubert-type shear test apparatus installed now at VUB. We thank L. Deriemaeker at VUB and C. Gruber at Univ. Maine for technical lab support and set-up construction. This work benefited from fruitful discussions with J. Kavanagh, S. Burchardt, M. Abdelmalak, B. van Wyk de Vries, P. Grosse and many others.

## References

Abdelmalak, M.M., Bulois, C., Mourgues, R., Galland, O., Legland, J.B., Gruber, C., 2016. Description of new dry granular materials of variable cohesion and friction coefficient: Implications for laboratory modeling of the brittle crust. Tectonophysics 684, 39–51. https://doi.org/10.1016/j.tecto.2016.03.003

Adam, J., Klinkmüller, M., Schreurs, G., Wieneke, B., 2013. Quantitative 3D strain analysis in analogue experiments simulating tectonic deformation: Integration of X-ray computed tomography and digital volume correlation techniques. J. Struct. Geol. 55, 127–149. https://doi.org/10.1016/j.jsg.2013.07.011

Adam, J., Urai, J.L., Wieneke, B., Oncken, O., Pfeiffer, K., Kukowski, N., Lohrmann, J., Hoth, S., van der Zee, W., Schmatz, J., 2005. Shear localisation and strain distribution during tectonic faulting - New insights from granular-flow experiments and high-resolution optical image correlation techniques. J. Struct. Geol. 27, 299–301. https://doi.org/10.1016/j.jsg.2004.08.008

Barenblatt, G.I., 2003. Scaling. Cambridge University Press.

Bertelsen, H.S., Rogers, B.D., Galland, O., Dumazer, G., Benanni, A., 2018. Laboratory

1176 modeling of coeval brittle and ductile deformation during magma emplacement into
1177 viscoelastic rocks. Front. Earth Sci. 6. https://doi.org/10.3389/feart.2018.00199
1178 Byerlee, J., 1978. Friction of rocks. Pure Appl. Geophys. 116, 615–626.
1179 https://doi.org/10.1007/BF00876528
1180 Byerlee, J.D., 1968. Brittle-ductile transition in rocks. J. Geophys. Res. 73, 4741–4750.
1181 https://doi.org/10.1029/JB073i014p04741
1182 Byrne, P.K., Holohan, E.P., Kervyn, M., Van Wyk de Vries, B., Troll, V.R., 2015. Analogue
1183 modelling of volcano flank terrace formation on Mars. Geol. Soc. Spec. Publ. 401, 185–
1184 202. https://doi.org/10.1144/SP401.14
1185 Byrne, P.K., Holohan, E.P., Kervyn, M., Van Wyk de Vries, B., Troll, V.R., Murray, J.B.,
1186 2013. A sagging-spreading continuum of large volcano structure. Geology 41, 339–342.
1187 https://doi.org/10.1130/G33990.1
1188 Cruz, L., Malinski, J., Wilson, A., Take, W.A., Hilley, G., 2010. Erosional control of the
1189 kinematics and geometry of fold-and-thrust belts imaged in a physical and numerical
1190 sandbox. J. Geophys. Res. Solid Earth 115, 1–15. https://doi.org/10.1029/2010JB007472
1191 Cubas, N., Barnes, C., Maillot, B., 2013. Inverse method applied to a sand wedge: Estimation
1192 of friction parameters and uncertainty analysis. J. Struct. Geol. 55, 101–113.
1193 https://doi.org/10.1016/j.jsg.2013.07.003
1194 Davy, P., Cobbold, P.R., 1991. Experiments on shortening of a 4-layer model of the
1195 continental lithosphere. Tectonophysics 188, 1–25. https://doi.org/10.1016/0040-
1196 1951(91)90311-F
1197 Delcamp, A., van Wyk de Vries, B., James, M.R., 2008. The influence of edifice slope and
1198 substrata on volcano spreading. J. Volcanol. Geotherm. Res. 177, 925–943.
1199 https://doi.org/10.1016/j.jvolgeores.2008.07.014
1200 Donnadieu, F., Merle, O., Besson, J.C., 2001. Volcanic edifice stability during cryptodome
1201 intrusion. Bull. Volcanol. 63, 61–72. https://doi.org/10.1007/s004450000122
1202 Dooley, T.P., Schreurs, G., 2012. Analogue modelling of intraplate strike-slip tectonics: A
1203 review and new experimental results. Tectonophysics 574–575, 1–71.
1204 https://doi.org/10.1016/j.tecto.2012.05.030
1205 Eisenstadt, G., Sims, D., 2005. Evaluating sand and clay models: Do rheological differences
1206 matter? J. Struct. Geol. 27, 1399–1412. https://doi.org/10.1016/j.jsg.2005.04.010
1207 Finot, E., Lesniewska, E., Goudonnet, J.P., Mutin, J.C., Domenech, M., At Kadi, A., 2001.
1208 Correlating surface forces with surface reactivity of gypsum crystals by atomic force
1209 microscopy. Comparison with rheological properties of plaster. Solid State Ionics 141–

142, 39–46. https://doi.org/10.1016/S0167-2738(01)00718-4

Galland, O., Bertelsen, H.S., Guldstrand, F., Girod, L., Johannessen, R.F., Bjugger, F., Burchardt, S., Mair, K., 2016. Application of open-source photogrammetric software MicMac for monitoring surface deformation in laboratory models. J. Geophys. Res. Earth 1–21. https://doi.org/10.1002/2015JB012755.

Galland, O., Burchardt, S., Hallot, E., Mourgues, R., Bulois, C., 2014. Dynamics of dikes versus cone sheets in volcanic systems. J. Geophys. Res. Solid Earth 119, 6178–6192. https://doi.org/10.1002/2014JB011059.Received

Galland, O., Cobbold, P.R., Hallot, E., de Bremond d'Ars, J., Delavaud, G., 2006. Use of vegetable oil and silica powder for scale modelling of magmatic intrusion in a deforming brittle crust. Earth Planet. Sci. Lett. 243, 786–804. https://doi.org/10.1016/j.epsl.2006.01.014

Galland, O., Holohan, E.P., van Wyk de Vries, B., Burchardt, S., 2018. Laboratory Modelling of Volcano Plumbing Systems: A Review, in: Breitkreuz, C., Rocchi, S. (Eds.), Physical Geology of Shallow Magmatic Systems - Dykes, Sills and Laccoliths. Springer Berlin Heidelberg, pp. 147–214.

Galland, O., Planke, S., Neumann, E.R., Malthe-Sorenssen, A., 2009. Experimental modelling of shallow magma emplacement: Application to saucer-shaped intrusions. Earth Planet. Sci. Lett. 277, 373–383. https://doi.org/10.1016/j.epsl.2008.11.003

Gibbings, J.C., 2011. Dimensional analysis. Springer, London.

Gomes, C.J.S., Caldeira, J.N.M., Freitas, A.R., 2006. The influence of different colours on the mechanical behaviour of quartz sand – first results. Ouro Preto Minas Gerais 35, 400–0.

Graveleau, F., Malavieille, J., Dominguez, S., 2012. Experimental modelling of orogenic wedges: A review. Tectonophysics 538–540, 1–66. https://doi.org/10.1016/j.tecto.2012.01.027

Grosse, P., Poppe, S., Delcamp, A., van Wyk de Vries, B., Kervyn, M., 2020. Volcano growth versus deformation by strike-slip faults: Morphometric characterization through analogue modelling. Tectonophysics 228411. https://doi.org/10.1016/j.tecto.2020.228411

Herbert, J.W., Cooke, M.L., Souloumiac, P., Madden, E.H., Mary, B.C.L., Maillot, B., 2015. The work of fault growth in laboratory sandbox experiments. Earth Planet. Sci. Lett. 432, 95–102. https://doi.org/10.1016/j.epsl.2015.09.046

Holland, M., van Gent, H., Bazalgette, L., Yassir, N., Hoogerduijn Strating, E.H., Urai, J.L., 2011. Evolution of dilatant fracture networks in a normal fault - Evidence from 4D

model experiments. Earth Planet. Sci. Lett. 304, 399–406. https://doi.org/10.1016/j.epsl.2011.02.017

Holohan, E.P., Van Wyk de Vries, B., Troll, V.R., 2008. Analogue models of caldera collapse in strike-slip tectonic regimes. Bull. Volcanol. 70, 773–796. https://doi.org/10.1007/s00445-007-0166-x

Holohan, E.P., Walter, T.R., Schöpfer, M.P.J., Walsh, J.J., Van Wyk De Vries, B., Troll, V.R., 2013. Origins of oblique-slip faulting during caldera subsidence. J. Geophys. Res. Solid Earth 118, 1778–1794. https://doi.org/10.1002/jgrb.50057

Hubbert, M.K., 1951. Mechanical basis for certain familiar geologic structures. Bull. Geol. Soc. Am. 62, 355–372. https://doi.org/10.1130/0016-7606(1951)62[355:MBFCFG]2.0.CO;2

Hubbert, M.K., 1945. Strength of the Earth. Am. Assoc. Pet. Geol. Bull. 29, 1630–1653.

Hubbert, M.K., 1937. Theory of scale models as applied to the study of geologic structures. GSA Bull. 48, 1459–1520.

J. C. Jaeger, N. G.W. Cook, andR. W.Z., 2007. Foundamentals of Rock Mechanics, The effects of brief mindfulness intervention on acute pain experience: An examination of individual difference. https://doi.org/10.1017/CBO9781107415324.004

Jaeger, J.C., Cook, N.G.W., Zimmerman, R.W., 2007. Fundamentals of Rock Mechanics, Cambridge University Press. https://doi.org/10.1017/CBO9781107415324.004

Jansen, H.A., 1895. Versuche über Getreidedruck in Silozellen. Zeitschrift des Vereiner Dtsch. Ingenieure 39, 1045–1049.

Kavanagh, J.L., Burns, A.J., Hilmi Hazim, S., Wood, E.P., Martin, S.A., Hignett, S., Dennis, D.J.C., 2018a. Challenging dyke ascent models using novel laboratory experiments: Implications for reinterpreting evidence of magma ascent and volcanism. J. Volcanol. Geotherm. Res. 354, 87–101. https://doi.org/10.1016/j.jvolgeores.2018.01.002

Kavanagh, J.L., Engwell, S., Martin, S., 2018b. A review of analogue and numerical modelling in volcanology. Solid Earth 9, 531–571. https://doi.org/10.5194/se-9-531-2018

Kervyn, M., Boone, M.N., de Vries, B. van W., Lebas, E., Cnudde, V., Fontijn, K., Jacobs, P., 2010. 3D imaging of volcano gravitational deformation by computerized X-ray micro-tomography. Geosphere 6, 482–498. https://doi.org/10.1130/ges00564.1

Kervyn, M., Ernst, G.G.J., Van Wyk De Vries, B., Mathieu, L., Jacobs, P., 2009. Volcano load control on dyke propagation and vent distribution: Insights from analogue modeling. J. Geophys. Res. 114, 26. https://doi.org/10.1029/2008JB005653

1278 Klinkmüller, M., Schreurs, G., Rosenau, M., Kemnitz, H., 2016. Properties of granular
1279 analogue model materials: A community wide survey. Tectonophysics 684, 23–38.
1280 https://doi.org/10.1016/j.tecto.2016.01.017
1281 Klinkmüller, M., Schreurs, G., Rosenau, M., Kemnitz, H., 2015. Properties of granular
1282 analogue model materials: A community wide survey. Tectonophysics 1–16.
1283 https://doi.org/10.1016/j.tecto.2016.01.017
1284 Krantz, R.W., 1991. Measurements of friction coefficients and cohesion for faulting and fault
1285 reactivation in laboratory models using sand and sand mixtures. Tectonophysics 188,
1286 203–207. https://doi.org/10.1016/0040-1951(91)90323-K
1287 Labuz, J.F., Zeng, F., Makhnenko, R., Li, Y., 2018. Brittle failure of rock: A review and
1288 general linear criterion. J. Struct. Geol. 112, 7–28.
1289 https://doi.org/10.1016/j.jsg.2018.04.007
1290 Lohrmann, J., Kukowski, N., Adam, J., Oncken, O., 2003. The impact of analogue material
1291 properties on the geometry, kinematics, and dynamics of convergent sand wedges. J.
1292 Struct. Geol. 25, 1691–1711. https://doi.org/10.1016/S0191-8141(03)00005-1
1293 Maillot, B., 2013. A sedimentation device to produce uniform sand packs. Tectonophysics
1294 593, 85–94. https://doi.org/10.1016/j.tecto.2013.02.028
1295 Mair, K., Frye, K.M., Marone, C., 2002. Influence of grain characteristics on the friction of
1296 granular shear zones. J. Geophys. Res. Solid Earth 107, ECV 4-1-ECV 4-9.
1297 https://doi.org/10.1029/2001jb000516
1298 Marti, J., Ablay, G.J., Redshaw, L.T., Sparks, R.S.J., 1994. Experimental study of collapse
1299 calderas. J. Geol. Soc. London. 151, 919–929.
1300 Mastin, L.G., Pollard, D.D., 1988. Surface deformation and shallow dike intrusion processes
1301 at Inyo Craters, Long Valley, California. J. Geophys. Res. 93, 13221–13235.
1302 https://doi.org/10.1029/JB093iB11p13221
1303 Mathieu, L., van Wyk de Vries, B., Holohan, E.P., Troll, V.R., 2008. Dykes, cups, saucers
1304 and sills: Analogue experiments on magma intrusion into brittle rocks. Earth Planet. Sci.
1305 Lett. 271, 1–13. https://doi.org/10.1016/j.epsl.2008.02.020
1306 Merle, O., 2015. The scaling of experiments on volcanic systems. Front. Earth Sci. 3, 1–15.
1307 https://doi.org/10.3389/feart.2015.00026
1308 Merle, O., Borgia, A., 1996. Scaled experiments of volcanic spreading. J. Geophys. Res. 101,
1309 13805. https://doi.org/10.1029/95JB03736
1310 Merle, O., Lénat, J.-F., 2003. Hybrid collapse mechanism at Piton de la Fournaise volcano,
1311 Reunion Island, Indian Ocean. J. Geophys. Res. 108, 1–11.

https://doi.org/10.1029/2002JB002014
Montanari, D., Agostini, A., Bonini, M., Corti, G., Del Ventisette, C., 2017. The use of empirical methods for testing granular materials in analogue modelling. Materials (Basel). 10, 1–18. https://doi.org/10.3390/ma10060635
Moulas, E., Sokoutis, D., Willingshofer, E., 2019. Pressure build-up and stress variations within the Earth's crust in the light of analogue models. Sci. Rep. 9, 1–8. https://doi.org/10.1038/s41598-018-38256-1
Mourgues, R., Cobbold, P.R., 2003. Some tectonic consequences of fluid overpressures and seepage forces as demonstrated by sandbox modelling. Tectonophysics 376, 75–97. https://doi.org/10.1016/S0040-1951(03)00348-2
Nieuwland, D.A., Urai, J.L., Knoop, M., 2000. In-situ stress measurements in model experiments of tectonic faulting. In: Lehner F.K., Urai J.L. (eds) Aspects of Tectonic Faulting. Springer, Berlin, Heidelberg.
Paguican, E.M.R., van Wyk de Vries, B., Lagmay, A.M.F., 2014. Hummocks: How they form and how they evolve in rockslide-debris avalanches. Landslides 11, 67–80. https://doi.org/10.1007/s10346-012-0368-y
Panien, M., Schreurs, G., Pfiffner, A., 2006. Mechanical behaviour of granular materials used in analogue modelling: insights from grain characterisation, ring-shear tests and analogue experiments. J. Struct. Geol. 28, 1710–1724. https://doi.org/10.1016/j.jsg.2006.05.004
Paterson, M.S., Wong, T., 2005. Experimental rock deformation-the brittle field, 2nd ed. Springer Science & Business Media.
Poppe, S., Holohan, E.P., Galland, O., Buls, N., Van Gompel, G., Keelson, B., Tournigand, P.-Y., Brancart, J., Hollis, D., Nila, A., Kervyn, M., 2019. An Inside Perspective on Magma Intrusion: Quantifying 3D Displacement and Strain in Laboratory Experiments by Dynamic X-Ray Computed Tomography. Front. Earth Sci. 7, 62. https://doi.org/10.3389/feart.2019.00062
Poppe, S., Holohan, E.P., Pauwels, E., Cnudde, V., Kervyn, M., 2015. Sinkholes, pit craters, and small calderas: Analog models of depletioninduced collapse analyzed by computed X-ray microtomography. Bull. Geol. Soc. Am. 127, 281–296. https://doi.org/10.1130/B30989.1
Poppe, S., Holohan, E.P., Rudolf, M., Rosenau, M., Galland, O., Delcamp, A., Van Gompel, G., Buls, N., Soens, B., Pohlenz, A., Mourgues, R., Kervyn, M., 2021. Mechanical test data of quartz sand, garnet sand, gypsum powder (plaster), kaolin and sand-plaster

mixtures used as granular analogue materials in geoscience laboratory experiments. https://doi.org/https://doi.org/10.5880/fidgeo.2021.005

Reber, J.E., Cooke, M.L., Dooley, T.P., 2020. What model material to use? A Review on rock analogs for structural geology and tectonics. Earth-Science Rev. 202, 103107. https://doi.org/10.1016/j.earscirev.2020.103107

Reid, H.F., 1911. The elastic-rebound theory of earthquakes. Univ. Calif. Publ. Dep. Geol. Sci.

Rincón, M., Márquez, A., Herrera, R., Alonso-Torres, A., Granja-Bruña, J.L., van Wyk de Vries, B., 2018. Contrasting catastrophic eruptions predicted by different intrusion and collapse scenarios. Sci. Rep. 8, 6178. https://doi.org/10.1038/s41598-018-24623-5

Ritter, M.C., Leever, K., Rosenau, M., Oncken, O., 2016. Scaling the sandbox—Mechanical (dis) similarities of granular materials and brittle rock. J. Geophys. Res. Solid Earth 121, 6863–6879. https://doi.org/10.1002/2016JB012915

Ritter, M.C., Rosenau, M., Oncken, O., 2018a. Growing Faults in the Lab: Insights Into the Scale Dependence of the Fault Zone Evolution Process. Tectonics 37, 140–153. https://doi.org/10.1002/2017TC004787

Ritter, M.C., Santimano, T., Rosenau, M., Leever, K., Oncken, O., 2018b. Sandbox rheometry: Co-evolution of stress and strain in Riedel– and Critical Wedge–experiments. Tectonophysics 722, 400–409. https://doi.org/10.1016/j.tecto.2017.11.018

Rivalta, E., Taisne, B., Bunger, A.P., Katz, R.F., 2015. A review of mechanical models of dike propagation: Schools of thought, results and future directions. Tectonophysics 638, 1–42. https://doi.org/10.1016/j.tecto.2014.10.003

Roche, O., Druitt, T.H., Merle, O., 2000. Experimental study of caldera formation. J. Geophys. Res. 105, 395. https://doi.org/10.1029/1999JB900298

Roche, O., Van Wyk De Vries, B., Druitt, T.H., 2001. Sub-surface structures and collapse mechanisms of summit pit craters. J. Volcanol. Geotherm. Res. 105, 1–18. https://doi.org/10.1016/S0377-0273(00)00248-1

Rosenau, M., Corbi, F., Dominguez, S., 2017. Analogue earthquakes and seismic cycles: Experimental modelling across timescales. Solid Earth 8, 597–635. https://doi.org/10.5194/se-8-597-2017

Rosenau, M., Lohrmann, J., Oncken, O., 2009. Shocks in a box: An analogue model of subduction earthquake cycles with application to seismotectonic forearc evolution. J. Geophys. Res. Solid Earth 114, 1–20. https://doi.org/10.1029/2008JB005665

Rudolf, M., Warsitzka, M., 2019. RST Evaluation - Scripts for analysing shear experiments

from the Schulze RST.pc01 ring shear tester.

Scheibert, J., Galland, O., Hafver, A., 2017. Inelastic deformation during sill and laccolith emplacement: Insights from an analytic elastoplastic model. J. Geophys. Res. Solid Earth 122, 923–945. https://doi.org/10.1002/2016JB013754

Schellart, W.P., 2000. Shear test results for cohesion and friction coefficients for different granular materials: Scaling implications for their usage in analogue modelling. Tectonophysics 324, 1–16. https://doi.org/10.1016/S0040-1951(00)00111-6

Schellart, W.P., Strak, V., 2016. A review of analogue modelling of geodynamic processes: Approaches, scaling, materials and quantification, with an application to subduction experiments. J. Geodyn. 100, 7–32. https://doi.org/10.1016/j.jog.2016.03.009

Scholz, C.H., 1972. Static fatigue of quartz. J. Geophys. Res. 77, 2104–2114. https://doi.org/10.1029/jb077i011p02104

Schöpfer, M.P.J., Abe, S., Childs, C., Walsh, J.J., 2009. The impact of porosity and crack density on the elasticity, strength and friction of cohesive granular materials: Insights from DEM modelling. Int. J. Rock Mech. Min. Sci. 46, 250–261. https://doi.org/10.1016/j.ijrmms.2008.03.009

Schöpfer, M.P.J., Childs, C., Manzocchi, T., 2013. Three-dimensional failure envelopes and the brittle-ductile transition. J. Geophys. Res. Solid Earth 118, 1378–1392. https://doi.org/10.1002/jgrb.50081

Schreurs, G., Buiter, S.J.H., Boutelier, D., Corti, G., Costa, E., Cruden, a. R., Daniel, J.-M., Hoth, S., Koyi, H. a., Kukowski, N., Lohrmann, J., Ravaglia, a., Schlische, R.W., Withjack, M.O., Yamada, Y., Cavozzi, C., Del Ventisette, C., Brady, J. a. E., Hoffmann-Rothe, a., Mengus, J.-M., Montanari, D., Nilforoushan, F., 2006. Analogue benchmarks of shortening and extension experiments. Geol. Soc. London, Spec. Publ. 253, 1–27. https://doi.org/10.1144/GSL.SP.2006.253.01.01

Schreurs, G., Buiter, S.J.H., Boutelier, J., Burberry, C., Callot, J.-P., Cavozzi, C., Cerca, M., Chen, J.-H., Cristallini, E., Cruden, A.R., Cruz, L., Daniel, J.-M., Da Poian, G., Garcia, V.H., Gomes, C.J.S., Grall, C., Guillot, Y., Guzmán, C., Hidayah, T.N., Hilley, G., Klinkmüller, M., Koyi, H.A., Lu, C.-Y., Maillot, B., Meriaux, C., Nilfouroushan, F., Pan, C.-C., Pillot, D., Portillo, R., Rosenau, M., Schellart, W.P., Schlische, R.W., Take, A., Vendeville, B., Vergnaud, M., Vettori, M., Wang, S.-H., Withjack, M.O., Yagupsky, D., Yamada, Y., 2016. Benchmarking analogue models of brittle thrust wedges. J. Struct. Geol. https://doi.org/10.1016/j.jsg.2016.03.005

Schreurs, G., Hanni, R., Panien, M., Vock, P., 2003. Analysis of analogue models by helical

X-ray computed tomography. Geol. Soc. London, Spec. Publ. 215, 213–223. https://doi.org/10.1144/GSL.SP.2003.215.01.20

Schultz, R.A., 1996. Relative scale and the strength and deformability of rock masses. J. Struct. Geol. 18, 1139–1149. https://doi.org/10.1016/0191-8141(96)00045-4

Schulze, D., 1994. Entwicklung und Anwendung eines neuartigen Ringschergerätes. Aufbereitungstechnik 35, 524–535.

Schweiger, A., Zimmermann, I., 1998. A new approach for the measurement of the tensile strength of powders. Powder Technol. 101, 1–9. https://doi.org/10.1016/S0032-5910(98)00117-X

Seropian, G., Stix, J., 2018. Monitoring and forecasting fault development at actively forming calderas: An experimental study. Geology 46, 23–26. https://doi.org/10.1130/G39551.1

Shea, T., van Wyk de Vries, B., 2008. Structural analysis and analogue modeling of the kinematics and dynamics of rockslide avalanches. Geosphere 4, 657–686. https://doi.org/10.1130/GES00131.1

Souloumiac, P., Maillot, B., Leroy, Y.M., 2012. Bias due to side wall friction in sand box experiments. J. Struct. Geol. 35, 90–101. https://doi.org/10.1016/j.jsg.2011.11.002

Tortini, R., Bonali, F.L., Corazzato, C., Carn, S.A., Tibaldi, A., 2014. An innovative application of the kinect in earth sciences: Quantifying deformation in analogue modelling of volcanoes. Terra Nov. 26, 273–281. https://doi.org/10.1111/ter.12096

Vachon, R., Hieronymus, C.F., 2017. Effect of host-rock rheology on dyke shape, thickness and magma overpressure. Geophys. J. Int. 208, 1414–1429. https://doi.org/10.1093/gji/ggw448

van Gent, H.W., Holland, M., Urai, J.L., Loosveld, R., 2010. Evolution of fault zones in carbonates with mechanical stratigraphy - Insights from scale models using layered cohesive powder. J. Struct. Geol. 32, 1375–1391. https://doi.org/10.1016/j.jsg.2009.05.006

van Mechelen, J.L.M., 2004. Strength of moist sand controlled by surface tension for tectonic analogue modelling. Tectonophysics 384, 275–284. https://doi.org/10.1016/j.tecto.2004.04.003

Van Wyk De Vries, B., Merle, O., 1998. Extension induced by volcanic loading in regional strike-slip zones. Geology. https://doi.org/10.1130/0091-7613(1998)026<0983:EIBVLI>2.3.CO;2

Voight, B., Elsworth, D., 1997. Failure of volcano slopes. Géotechnique 47, 1–31. https://doi.org/10.1680/geot.1997.47.1.1

Warsitzka, M., Ge, Z., Schönebeck, J.-M., Pohlenz, A., Kukowski, N., 2019. Ring-shear test data of foam glass beads used for analogue experiments in the Helmholtz Laboratory for Tectonic Modelling (HelTec) at the GFZ German Research Centre for Geosciences in Potsdam and the Institute of Geosciences, Friedrich Schiller University. https://doi.org/10.5880/GFZ.4.1.2019.002

Williams, S.C., 1988. The shear strength of gypsum single crystals on three cleavage planes. Tectonophysics 148, 163–173. https://doi.org/10.1016/0040-1951(88)90168-0

Zorn, E.U., Walter, T.R., Heap, M.J., Kueppers, U., 2020. Insights into lava dome and spine extrusion using analogue sandbox experiments. Earth Planet. Sci. Lett. 551, 116571. https://doi.org/10.1016/j.epsl.2020.116571

Zwaan, F., Schreurs, G., 2017. How oblique extension and structural inheritance influence rift segment interaction: Insights from 4D analog models. Interpretation 5, SD119–SD138. https://doi.org/10.1190/INT-2016-0063.1

1463

## SUPPLEMENTARY MATERIAL

### Normal load correction of direct shear test data

Part of the normal stress applied on the horizontal shear plane by the sample and additional loads in the upper cylinder is counteracted by friction between the granular sample and the plastic of the upper cylinder, also called the 'silo effect' or 'Janssen effect' (Jansen 1895). The method of Mourgues and Cobbold (2003) was used to measure the silo effect empirically, and correct the normal loads used to construct the failure envelopes (Figure 8 in main text). The upper cylinder was suspended <1 mm above a precision balance, each granular material was emplaced and compacted in the same manner as for complete direct shear tests to obtain the same densities (Table 2 in main text). The weight then registered by the balance was the effective normal load exerted on the failure plane in the direct shear tests. These normal load measurements were repeated at least three times for each applied normal load (Figure S1). For all materials, these measurements fell on a linear trend with a slope lower than that of the zero-friction diagonal line. To ensure reproducibility of the measurements, more runs were added if necessary to reach a $r^2$ >0.990 linear regression value of the data in a measured normal load vs. theoretical normal load (i.e. zero friction between material and cylinder wall) plot.

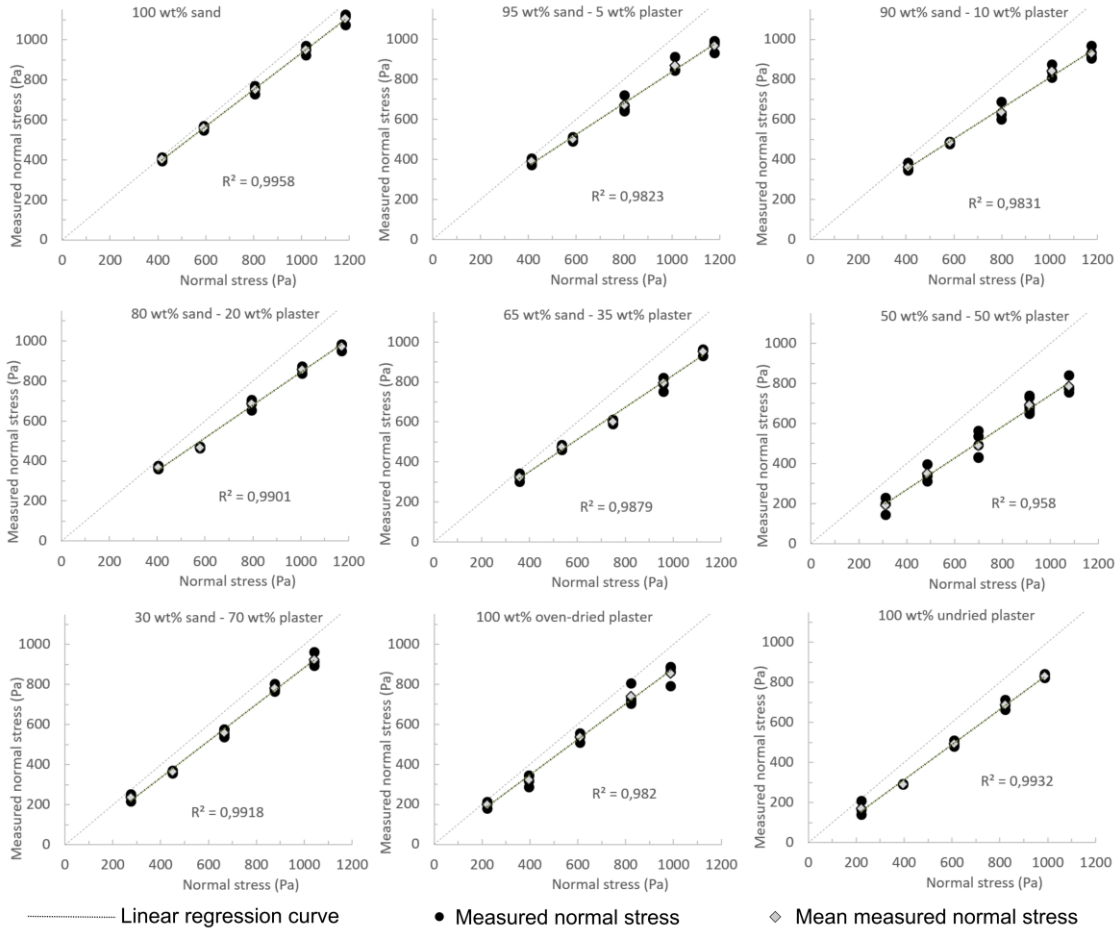


**Figure S1** – Measured normal stress versus theoretical (i.e. zero-friction) normal stress ($\sigma_n$) plots for sand and plaster and their mixtures. The means were used as normal load values in the direct shear test results that reconstruct the failure envelopes of Figure 6.